



Shrub decline and expansion of wetland vegetation revealed by very high resolution land cover change detection in the Siberian lowland tundra

Rúna Í. Magnússon^{a,*}, Juul Limpens^a, David Kleijn^a, Ko van Huissteden^b, Trofim C. Maximov^{c,d}, Sylvain Lobry^e, Monique M.P.D. Heijmans^a

^a Plant Ecology and Nature Conservation Group, Wageningen University & Research, Wageningen, the Netherlands

^b Department of Earth Sciences, Faculty of Science, Vrije Universiteit, Amsterdam, the Netherlands

^c Institute for Biological Problems of the Cryolithosphere, Siberian Branch Russian Academy of Sciences, Yakutsk, Russia

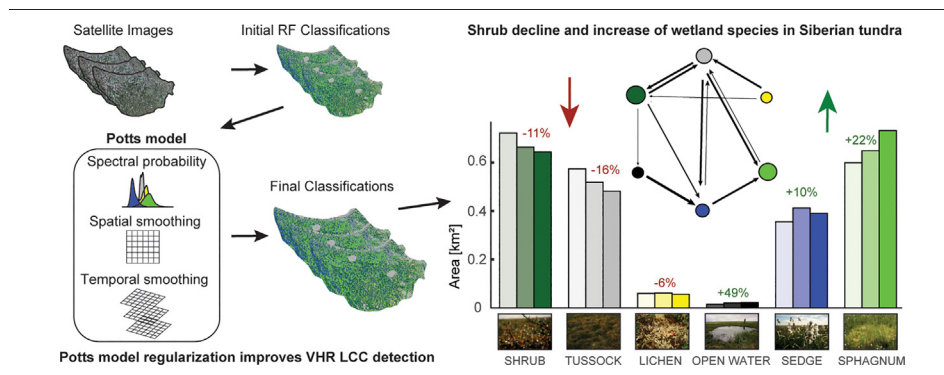
^d North-Eastern Federal University, Yakutsk, Russia

^e LIPADE, Université de Paris, Paris, France

HIGHLIGHTS

- The Indigirka Lowlands show a wetting trend and divergent greening/browning.
- VHR data revealed shrub decline and surface water and wetland vegetation expansion.
- Thermokarst and terrain wetting explain local shrub decline and tundra browning.
- Accurate VHR change detection is essential for monitoring of Arctic ecosystems.

GRAPHICAL ABSTRACT



ARTICLE INFO

Article history:

Received 30 October 2020

Received in revised form 10 March 2021

Accepted 28 March 2021

Available online 1 April 2021

Editor: Damia Barcelo

Keywords:

Siberian lowland tundra
Arctic greening
Permafrost
Land cover change
Potts model
Vegetation succession

ABSTRACT

Vegetation change, permafrost degradation and their interactions affect greenhouse gas fluxes, hydrology and surface energy balance in Arctic ecosystems. The Arctic shows an overall “greening” trend (i.e. increased plant biomass and productivity) attributed to expansion of shrub vegetation. However, Arctic shrub dynamics show strong spatial variability and locally “browning” may be observed. Mechanistic understanding of greening and browning trends is necessary to accurately assess the response of Arctic vegetation to a changing climate. In this context, the Siberian Arctic is an understudied region. Between 2010 and 2019, increased browning (as derived from the MODIS Enhanced Vegetation Index) was observed in the Eastern Siberian Indigirka Lowlands. To support interpretation of local greening and browning dynamics, we quantified changes in land cover and transition probabilities in a representative tundra site in the Indigirka Lowlands using a timeseries of three very high resolution (VHR) (0.5 m) satellite images acquired between 2010 and 2019. Using spatiotemporal Potts model regularization, we substantially reduced classification errors related to optical and phenological inconsistencies in the image material. VHR images show that recent browning was associated with declines in shrub, lichen and tussock vegetation and increases in open water, sedge and especially *Sphagnum* vegetation. Observed formation and expansion of small open water bodies in shrub dominated vegetation suggests abrupt thaw of ice-rich permafrost. Transitions from open water to sedge and *Sphagnum*, indicate aquatic succession upon disturbance. The overall shift towards open water and wetland vegetation suggests a wetting trend, likely associated with permafrost degradation. Landsat data confirmed widespread expansion of surface water throughout the Indigirka

* Corresponding author.

E-mail address: runa.magnusson@wur.nl (R.Í. Magnússon).

Lowlands. However, the increase in the area of small water bodies observed in VHR data was not visible in Landsat-derived surface water data, which suggests that VHR data is essential for early detection of small-scale disturbances and associated vegetation change in permafrost ecosystems.

© 2021 The Author(s). Published by Elsevier B.V. This is an open access article under the CC BY license (<http://creativecommons.org/licenses/by/4.0/>).

1. Introduction

The Arctic is warming twice as fast as the global average, resulting in release of greenhouse gases (GHG) from thawing permafrost (Meredith et al., 2019; Schuur et al., 2015) and widespread vegetation change (Pearson et al., 2013). Shrubs in particular have been observed to expand across the Arctic, resulting in an overall greening trend (i.e. an increase in Normalized Difference Vegetation Index, NDVI) as evident from remote sensing studies (Bhatt et al., 2017; Epstein et al., 2013; Frost et al., 2020; Myers-Smith et al., 2015; Tape et al., 2006). Increased carbon uptake in shrub biomass may partially mitigate greenhouse gas (GHG) emissions from thawing permafrost (Epstein et al., 2012; McGuire et al., 2018). However, shrubs do not expand everywhere and show divergent responses to climatic drivers (Bjorkman et al., 2020; Epstein et al., 2013; Lin et al., 2012; Martin et al., 2017; Naito and Cairns, 2011). Browning (i.e., a decrease in NDVI) is increasingly observed in various locations across the Arctic (Bhatt et al., 2017; Frost et al., 2020). The Russian Arctic is an underrepresented region in the context of ground studies and high-resolution remote sensing of Arctic shrub expansion in English scientific literature (Bjorkman et al., 2020; Elmendorf et al., 2012; Martin et al., 2017), despite harboring approximately half of the total circumpolar area of shrub and tussock-shrub dominated tundra ecosystems (Raynolds et al., 2019). Dendrochronological studies in the Russian Arctic have shown a positive response of dwarf shrubs to climate warming (Blok et al., 2011b; Forbes et al., 2010), supported by several remote sensing studies that report increased NDVI and shrub expansion (Forbes et al., 2010; Frost et al., 2014; Lin et al., 2012; Nitze and Grosse, 2016). However, browning related to permafrost degradation (Nitze and Grosse, 2016) and increases in open water and wetland vegetation (Lin et al., 2012) have also been reported locally in the Russian Arctic. Mechanistic understanding of the drivers and impacts of browning is necessary to predict the response of this understudied region to a warming climate.

The lowland tundra of north-eastern Siberia is of particular interest in the context of Arctic climate change, due to its high ground ice content (Iwahana et al., 2014; Nitzbon et al., 2020; Olefeldt et al., 2016) and distinctly continental climate with high summer temperatures (van der Molen et al., 2007), giving it the potential for rapid permafrost degradation (Nitzbon et al., 2020). This can result in disturbance of vegetation (Abbott et al., 2016), particularly in poorly drained lowland sites (Loranty et al., 2018a). As such, surface wetting as a result of abrupt thaw has been suggested as a potential cause of local Arctic browning (Phoenix and Bjerke, 2016; Raynolds and Walker, 2016), among other drivers such as wildfires, outbreaks of insects and pathogenic fungi and increased variability in winter temperature and precipitation (Bjerke et al., 2017; Phoenix and Bjerke, 2016). An estimated 20% of the total circumpolar area contains ice-rich permafrost and is sensitive to abrupt thaw (Olefeldt et al., 2016). These findings illustrate the need to take abrupt thaw in ice-rich permafrost into consideration as a potential control on shrub dynamics and the Arctic greening trend. Earlier research in the Siberian lowland tundra suggests that shrub vegetation can be replaced rapidly by graminoids and peat moss vegetation through formation of small-scale, waterlogged permafrost collapses in previously dwarf shrub dominated vegetation (Li et al., 2017; Magnússon et al., 2020; Nauta et al., 2015). Comparable successions towards sedge and peat moss dominated vegetation have been observed as a response to ice-wedge degradation (Jorgenson et al., 2015; Kanevskiy et al., 2017). Such successions affect the GHG balance

(Turetsky et al., 2020) and surface energy balance (Loranty et al., 2018a) of permafrost ecosystems.

Acquisition of satellite images in the Arctic is often limited by low sun-angles, short growing seasons, high cloud frequencies and logistic challenges in the acquisition of ground reference data (Beamish et al., 2020; Myers-Smith et al., 2020). Furthermore, greening dynamics derived from satellite-based vegetation indices such as NDVI are influenced by the spatial scale of satellite images and timing of acquisition, as well as non-vegetation related terrain properties such as water and snow dynamics. As a result, it remains a challenge to relate large scale greening dynamics to actual vegetation processes in Arctic ecosystems (Myers-Smith et al., 2020) and vegetation indices do not always capture actual vegetation cover dynamics (Loranty et al., 2018b). Increasing availability of very high resolution (VHR) satellite images have substantially advanced monitoring studies of Arctic ecosystems and interpretation of local greening dynamics, but are subject to similar heterogeneity in optical properties and seasonal timing (Beamish et al., 2020). This limits the potential for traditional change detection based on post-classification comparison, as misclassifications in individual images and spectral inconsistencies among images introduce false positives and negatives in change detection (Aspinall and Hill, 1997; Serra et al., 2003; Singh, 1989). Markov Random Field (MRF) regularization, introduced in computer vision by Geman and Geman (1984), is a potential remedy for false positives and false negatives in change detection using heterogeneous image time series. This method uses the inherent spatial relations between pixels in an image to enhance consistency of classification and can be extended to include temporal relations between pixels to improve classification consistency in timeseries (Cai et al., 2014; Gómez et al., 2016; Solberg et al., 1996; Wang et al., 2015; Wehmann and Liu, 2015).

To advance our process-based understanding of Arctic greening and browning dynamics, we relate larger scale trends in vegetation greenness and surface water area to high resolution land cover changes of typical tundra vegetation types. Based on field observations and earlier studies, we expected coarse resolution browning trends in the Indigirka Lowlands to be associated with expansion of surface water bodies at the expense of shrub vegetation, followed by succession of aquatic species (Li et al., 2017; Magnússon et al., 2020; Nauta et al., 2015). First, we derived trends in vegetation greenness as measured by the Enhanced Vegetation Index (EVI) from the MODIS record and trends in surface water area from the Landsat-based Global Surface Water Map (Pekel et al., 2016) for the entire Indigirka Lowlands region. For a smaller study area, we classified a time series (2010–2019) of three VHR (0.5 m) GeoEye-1 and WorldView-2 satellite images into land cover classes representing distinct types of tundra vegetation (a.o. shrub-dominated vegetation). Our approach based on the use of VHR data has the advantage that small-scale disturbances on shorter timescales can be captured that may not be evident from moderate (e.g. Landsat) to coarse resolution (e.g. MODIS) data (Grosse et al., 2008; Muster et al., 2013). We applied the Potts model (Potts, 1952), a simple and widely used MRF regularization method, supported by validation data of areas of known change or no change in land cover. This allowed us to optimize and quantify accuracy of change detection using satellite images from different sensors and phenological stages. By explicitly quantifying not only net changes but also rates and potential trajectories of vegetation change, we contribute to process-based knowledge on shrub dynamics. We thereby improve our understanding of underlying mechanisms of vegetation change and greening in this understudied Arctic region.

2. Data & methods

2.1. Study area

We studied greening and browning trends and surface water dynamics in the Indigirka Lowlands region (108,786 km²) in North-Eastern Siberia. Its main landscape units are drained thaw lake basins or “alases”, river floodplains, inter-alas Yedoma ridges and coastal marshlands (Fedorov et al., 2018). Vegetation in this low elevation region consists primarily of tundra vegetation, transitioning to taiga vegetation in the south (Fig. 1a). We quantified land cover change in a focus area consisting of a single alas in the “Kytalyk” Nature Reserve in the Indigirka Lowlands in north-eastern Siberia (70°49'N, 147°29'E) near the town of Chokurdakh (Fig. 1). This area is characterized by a shallow active layer overlying continuous permafrost of over 300 m thickness (Van Huissteden et al., 2005). Mean annual temperature is −13.4 °C, with an average July temperature of 10.3 °C (1981–2010). Mean annual precipitation is 196 mm, with 76 mm falling in June to August (1981–2010) (Trouet and Van Oldenborgh, 2013). The Circumpolar Arctic Vegetation Map (CAVM) classifies this site as a mix of tussock-sedge tundra (type G4), erect dwarf shrub tundra and sedge-moss wetland, which are typical vegetation classes for low elevation areas with relatively high summer temperatures and high NDVI (Raynolds et al., 2019). This combination of landform, climate and vegetation types is representative for a major part of coastal north-eastern Siberia (Fedorov et al., 2018; Raynolds et al., 2019). Ground ice content

around the study site is high (75 vol% on average in the top 1 to 2 m of soil) (Iwahana et al., 2014; Wang et al., 2019) and the studied alas shows both ice-wedge degradation and formation of shallow, irregularly shaped thaw ponds most likely resulting from degradation of lenticular ground ice (Magnússon et al., 2020; van Huissteden, 2020). Within the study area, elevated yedoma remnants and pingos are characterized by tussock-sedge (*Eriophorum vaginatum*) vegetation. Lower elevation areas such as alases are characterized by slightly elevated shrub patches dominated by *Betula nana*, lichens and mosses, interspersed with waterlogged depressions characterized by *Eriophorum angustifolium*, *Carex* spp. and *Sphagnum* spp. In the study area, these waterlogged depressions tend to be orientated perpendicular to the local terrain slope, forming wide diffuse drainage lines of irregular width (see e.g. linear patterns in Fig. 1c directed towards the river). Lastly, floodplains are characterized by willow vegetation, grasslands and bare ground (Siewert et al., 2015). We selected our study site as a single, older (Fig. 1b) alas, excluding rivers, human infrastructure, surrounding inter-alas yedoma ridges and areas subject to occasional flooding due to high river discharge. This resulted in a total area of 2.33 km² (see Fig. 1c).

2.2. Regional dynamics of vegetation greenness and surface water

To inventory greening/browning trends and surface water dynamics in the wider Indigirka lowlands region, we evaluated Terra and Aqua MODIS Enhanced Vegetation Index (EVI) products for 2000 to 2019

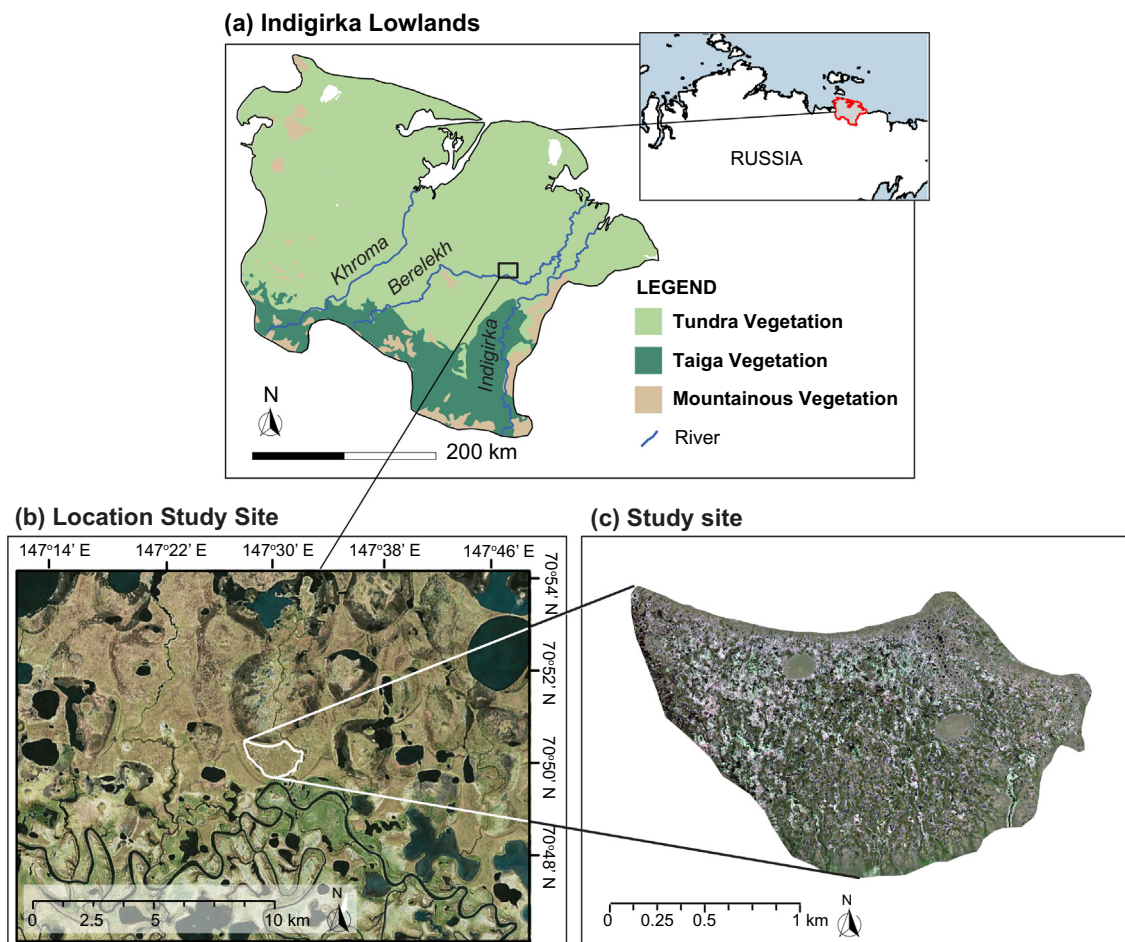


Fig. 1. Location of the study area. (a) Location of the Indigirka Lowlands and main vegetation zones and rivers as defined in Fedorov et al. (2018) (b) Landsat image of the study region, which contains numerous small lakes, streams and alases, as well as larger lakes in the north. The selected alas represents an older episode of thaw lake drainage. The bottom half of the image shows the meandering Berelekh river and its floodplain. The study area is bordered by Pleistocene yedoma ridges in the southeast and southwest. Image courtesy of ESRI/DigitalGlobe. (c) WorldView-2 satellite image of the study area. Worldview © MAXAR 2019. Light colours represent *Sphagnum* carpets, darker spots are surface water features. The two circular features are pingos with tussock vegetation. Numerous small ponds, areas with polygonal tundra and several diffuse drainage lines are visible.

(products MOD13Q1 and MYD13Q1 v.006) (Didan, 2015a, 2015b). Similar to NDVI, EVI uses the ratio of red and near infrared reflectance, but applies corrections for variable aerosol concentrations and soil brightness (Didan, 2015b). For each year, we selected all 16-day composite 250 m resolution EVI images in June, July and August and calculated the annual maximum EVI to represent the peak growing season over the entire Indigirka Lowlands region (Fig. 1a). Using the MODIS pixel reliability product we selected only “high” and “useful” quality pixels. Maximum EVI generally fell in late July. We calculated linear trends in maximum EVI over time for the entire MODIS observation period (2000–2019) as well as the period (2010–2019) that was used for land cover change analysis. Trends were quantified as slope coefficients over time using ordinary least squares linear regression. To assess significance of trends, slope coefficients were estimated using an ordinary bootstrap method with replacement ($n = 100$). We used the adjusted bootstrap percentile (Davison and Hinkley, 1997) to calculate the 95% confidence interval (CI) of the slope estimate. EVI trends were reported as significant if the 95% CI did not include zero. We then compared EVI trends within the smaller study area to those in the entire Indigirka lowlands region. Used software and packages are listed in text S2. In addition, we quantified the dynamics of various types of surface water (permanent, seasonal and ephemeral) for the Indigirka Lowlands as derived from the Global Surface Water Map (GSWM). The GSWM contains 30 m resolution data on the presence and change dynamics of surface water as derived from the Landsat record between the 1984–1999 and 2000–2019 periods (Pekel et al., 2016).

2.3. Satellite data and distinguished land cover classes

To assess recent changes in land cover at our site in high spatial detail, we used three VHR, cloud-free satellite images from different sensors with different timing of acquisition within the growing season. We used a GeoEye-1 image from mid-August 2010, a WorldView-2 image from early July 2015 and a WorldView-2 image from early August 2019, with comparable resolution and bandwidths (see Table S1). All three images were pan-sharpened to 0.5 m resolution using the Gram-Schmidt algorithm in ArcMap 10.6.1 (ESRI, 2019). Images were georeferenced manually, using permanent and recognizable features in the landscape. All three images achieved subpixel (0.5 m) georeferencing accuracy. Correction to top-of-atmosphere reflectance was performed for all three products according to Podger et al. (2011) for GeoEye-1 and Updike and Comp (2010) for WorldView-2. Since training data were available for each individual year, atmospheric correction was not deemed necessary for classification purposes (Song et al., 2001).

To study land cover dynamics, we distinguished six specific land cover classes (Table 1). Similar distinctions for this study area have been used by Siewert et al. (2015) and Li et al. (2017). Distinctions were made between vegetation dominated by woody plants (dwarf shrubs), aquatic sedge communities (sedges), tussock sedge communities (tussock), peat mosses (*Sphagnum*) and lichens (lichen), with open water areas representing a final land cover class. The “open water” class included areas of mud with no considerable amount of living vegetation, since fluctuations in water level may cause large differences in open water extent in alases (Desyatkin et al., 2014; Fedorov et al., 2014; Jones et al., 2009).

2.4. Ground reference data

We used training, validation and test data for our classification workflow, which were created as polygon shapefiles in ArcMap 10.6.1 (ESRI, 2019). Training sites were selected based on visual interpretation of satellite images by researchers familiar with the area. Wherever possible (i.e. sites showed no vegetation change), we selected the same pixels for all images to minimize inconsistencies in initial classification due to differences in training site selection. In support of classification,

we calculated Bhattacharyya distance (Bhattacharyya, 1946) as a metric of class separability based on the spectral data of training sites.

Validation sites were selected based on repeated photographs of plots with known coordinates from previous experiments in the study area (Li, 2017), including both areas with known changes in vegetation composition and areas with no change (Fig. S22). Photographs from the summer of 2011 were used for the 2010 image, while photographs from the same summer were available for 2015 and 2019. The same pixels were used in each year as validation sites. About 15% of pixels in the validation data showed a change in land cover class.

Test sites for 2019 were located in the field in August 2019 using a Real-Time Kinematic Global Navigation Satellite System (Hiper HR, TopCon, Tokyo, Japan) in a base and rover set-up using GPS and GLONASS satellites. The perimeter of 171 patches representing the land cover classes in Table 1 was recorded with sub-centimeter accuracy. Test sites for 2015 and 2010 were copied from the test sites for 2019 if visual inspection of the images showed no indication of land cover change. The same pixels were used for the test set in all three years to avoid inconsistency of accuracy assessment due to the use of different sets of pixels. Wherever possible, validation and test sites were selected as adjacent patches including patch borders to avoid validating and testing only against highly representative patch centers. Boundaries between land cover classes in the validation and test sites were assigned based on visual interpretation of species composition in the field or from reference photographs. The amount of area covered by training, validation and test sites is summarized in Table S2.

2.5. Classification and change detection

Image classification was performed in R version 3.6.2 (R Development Core Team, 2019). Images were co-registered using bilinear interpolation and classified based on the training data with a Random Forest (RF). The hyperparameters of the RF classifier (number of trees and the number of variables randomly sampled as candidates at each split) were empirically set to 500 and 2 respectively for maximum overall accuracy of classification using the validation data.

In support of land cover classification of spectrally and seasonally heterogeneous images we used a spatiotemporal implementation of the Potts model (Potts, 1952). Apart from class probabilities based on spectral data, the Potts model introduces a smoothing term based on the correspondence of a pixel's class with the classes of spatially adjacent pixels. We included an additional smoothing term representing the degree of correspondence of a pixel's class with the class values of temporally adjacent pixels (i.e., the same pixel in an earlier or later image). This way, the probability for a pixel belonging to a class that is different from its spatial neighbors, or different from the class it was assigned to in the previous or following image was reduced. After adjusting probabilities for each pixel in this way, the class of a pixel was set to that which then had the highest probability. This process was repeated using Iterated Conditional Modes (ICM) (Besag, 1986) optimization until a stable classification was reached. A detailed description of the classification algorithm is provided in supplementary text S1. Used software and packages are listed in text S2.

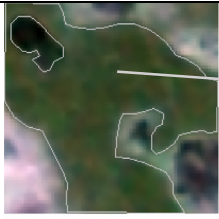



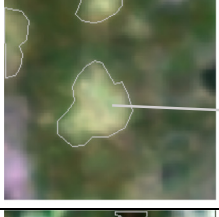

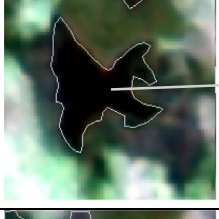





We set the weights assigned to the spatial and temporal smoothing terms (β_0 and β_1) for optimal change detection using the validation data. Classification was performed for a range of potential values for the spatial ($\beta_0 = 0$ –2 with steps of 0.2) and temporal ($\beta_1 = 0$ –3 with steps of 0.5) smoothing weights. For the resulting suite of optimized classifications, change detection performance indicators described in Section 2.6 were calculated to select the final, optimal classification. Our workflow is summarized visually in Fig. 2.

2.6. Accuracy assessment

Change detection accuracy was determined from change detection confusion matrices (Macleod and Congalton, 1998) per combination of

Table 1

Land cover classes used for this study. Examples are fragments (1:1500) of the 2015 WorldView-2 image to illustrate the appearance of the distinguished land cover classes. Fragments are pan-sharpened true color composites (red, green and blue band) of top-of-atmosphere reflectance values. Worldview © MAXAR, 2019. Photographs by Rúna Magnússon.

Name	Description	Main species	Example	Field Photograph
<i>Shrub</i>	Dwarf shrubs with moss and lichen understory, occurring on slightly elevated patches. Green shades in satellite images.	<i>Betula nana</i> , <i>Salix pulchra</i> , <i>Polytrichum</i> spp., <i>Dicranum</i> spp., <i>Flavocetraria cucullata</i> , <i>Cladonia</i> spp., <i>Peltigera</i> spp.		
<i>Tussock</i>	Mixed vegetation of tussock sedges, dwarf shrubs, mosses and lichens. Visible as light greyish areas in satellite images.	<i>Eriophorum vaginatum</i> , <i>Rhododendron tomentosum</i> , <i>Vaccinium vitis-idaea</i> , <i>Flavocetraria cucullata</i> , <i>Betula nana</i> , <i>Salix pulchra</i> , <i>Cladonia</i> spp., <i>Polytrichum</i> spp., <i>Dicranum</i> spp.		
<i>Lichen</i>	Lichen rich areas with little to no shrubs and/or tussock sedges. Visible as light yellow-green areas in satellite images.	<i>Flavocetraria cucullata</i> , <i>Cetraria</i> spp., <i>Cladonia</i> spp., <i>Vaccinium vitis-idaea</i> , occasionally <i>Betula nana</i> and <i>Salix pulchra</i> .		
<i>Open Water</i>	Areas with open water or mud with no considerable amount of living vegetation. Visible as dark areas in satellite images.	None. Occasionally with dead vegetation (mostly shrubs).		
<i>Sedge</i>	Wet areas dominated by sedges. Visible as dark green areas in satellite images.	Aquatic sedges, predominantly <i>Eriophorum angustifolium</i> , and <i>Carex aquatilis</i> .		
<i>Sphagnum</i>	Peat moss carpets. Visible as light white to green areas in satellite images.	<i>Sphagnum</i> mosses, predominantly <i>Sphagnum obtusum</i> and <i>Sphagnum squarrosum</i> , often with partial cover of dried out aquatic sedges.		

two images using the areas of known change and no-change from the validation data. Similar to conventional confusion matrices, these tabulate the predicted class transitions against the observed class transitions for each combination of two images. To assess the degree to which chosen parameters lead to over- or underestimation of change, we calculated Matthew's Correlation Coefficient (MCC) (Matthews, 1975) from a confusion matrix for a binary reclassification into change/no-change areas. The MCC is a more reliable metric than overall accuracy in case of binary classification of unbalanced datasets (Chicco and Jurman, 2020) and is calculated from the relative number of true positives (TP), true negatives (TN), false positives (FP) and false negatives (FN) in the confusion matrix. An MCC of +1 indicates perfect prediction, 0 represents no better than random prediction and -1 represents a

perfect negative correlation between the prediction and the ground truth (Eq. (1)).

$$MCC = \frac{(TP * TN) - (FP * FN)}{\sqrt{(TP + FP) * (TP + FN) * (TN + FP) * (TN + FN)}} \quad (1)$$

In addition, from the change/no change confusion matrix we calculated the false discovery rate (FDR) of change detection as $\frac{FP}{FP + TP}$ and the false omission rate (FOR) as $\frac{FN}{FN + TN}$.

Final classification accuracy per individual image was calculated using a confusion matrix based on the predicted and observed class values for the test sites (Congalton, 1991). For reference, baseline

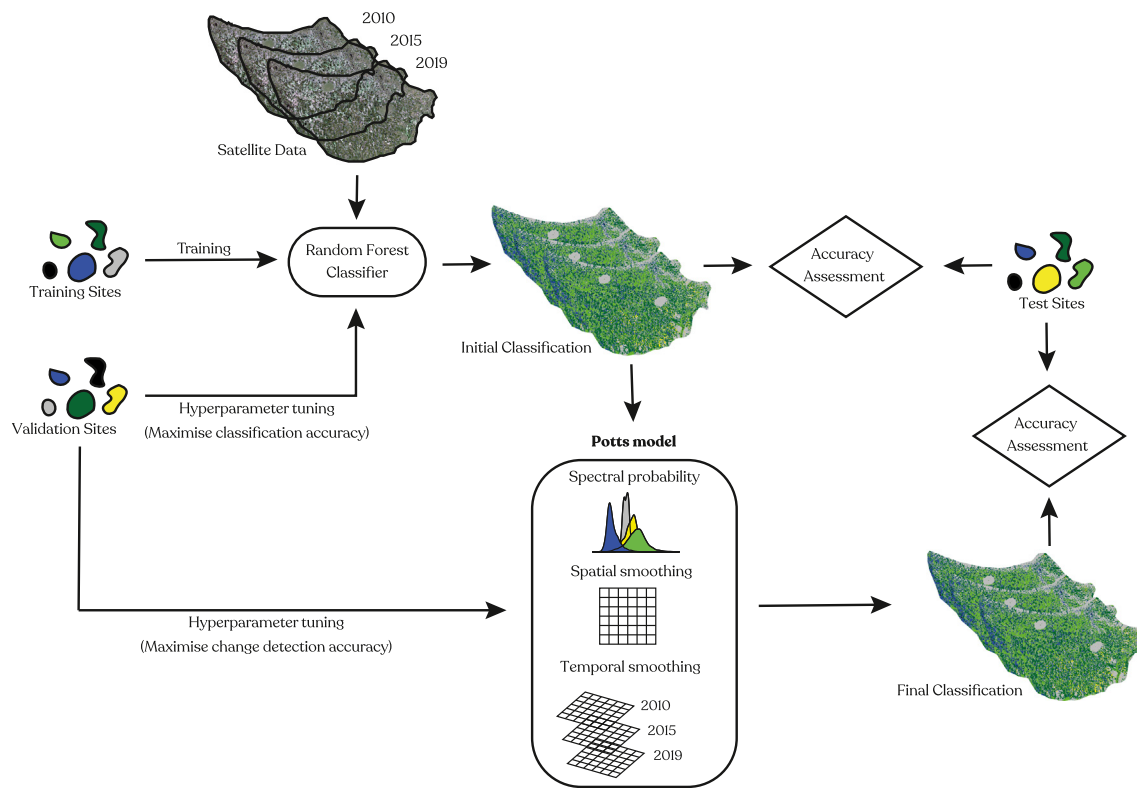


Fig. 2. Schematic representation of workflow used for satellite data classification. Initial classification was derived from a random forest classifier using the training data. The validation data were used to tune the random forest based on overall classification accuracy, and to select the hyperparameters for the Potts model based on accuracy of change detection. The accuracy of the resulting final classification and the initial classification were calculated from the test data.

accuracies for the initial RF classifications without Potts model regularization were determined in the same manner. We calculated the total area of land cover classes per year as well as net transitions for both time periods (2010–2015 and 2015–2019). Class transition probabilities were calculated according to Muller and Middleton (1994) per combination of two images.

3. Results

3.1. Trends in vegetation greening and terrain wetting in the Indigirka Lowlands

Over the entire MODIS observation period (2000–2019), the Indigirka Lowlands region showed no pronounced overall greening/browning (mean trend = $0.67\text{e}^{-3}\text{ yr}^{-1} \pm 0.09\text{e}^{-3}\text{ yr}^{-1}$). Of all pixels for which trends could be calculated, 12.29% showed significant greening and 2.26% showed significant browning. However, distinct spatial differences related to landscape heterogeneity were evident (Fig. 3b): mountainous vegetation (Fig. 1a) east of the Indigirka river and coastal tundra showed relatively strong greening. Particularly strong and divergent EVI trends were found around lakes and in alases. The Landsat-derived GSWM indicates a widespread increase in surface water between the periods 1984–1999 and 2000–2019, although not in the study area (Fig. 3a). The extent of permanent water features showed a relative increase of 9.96% and the extent of seasonal surface water increased more than eightfold (+846.70%). Increases in surface water appear concentrated in flood plains of major rivers and in alas terrain north of the river Berelekh and west of the river Khroma. Although no clear EVI trends were observed in the study area over the MODIS observation period (mean trend = $-0.86\text{e}^{-3}\text{ yr}^{-1} \pm 0.79\text{e}^{-3}\text{ yr}^{-1}$, Fig. 3b), intensified browning was observed over the study period 2010–2019 (mean trend = $-8.77\text{e}^{-3}\text{ yr}^{-1} \pm 2.57\text{e}^{-3}\text{ yr}^{-1}$) and EVI decreased

steadily (Fig. S26e). Similar increases in browning after 2010 were found across the Indigirka Lowlands (mean trend = $-1.99\text{e}^{-3}\text{ yr}^{-1} \pm 4.96\text{e}^{-3}\text{ yr}^{-1}$). 1.60% of pixels showed significant greening while 14.16% showed significant browning between 2010 and 2019. Variability in trends was high and particular sites, such as northern coastal lowlands, continued greening (Fig. 3c).

3.2. Optimization of very high resolution image classification

VHR image classification accuracy and change detection accuracy were improved substantially after Potts model regularization. Initial RF classifications achieved overall classification accuracies of 78% (2010), 91% (2015) and 82% (2019). Change detection accuracies were between 62% and 68% per image pair. MCCs were 0.27 (2010–2015), 0.26 (2015–2019) and 0.30 (2010–2019) (Table S8). Confusion matrices for baseline RF classifications (Table S6) and spectral separability plots (Figs. S1–S3, Tables S3–S5) indicate that the extent to which particular classes could be distinguished using only spectral data varied among images as well as classes. *Sphagnum* and shrub had high spectral separability and accuracy across images, whereas misclassifications were relatively frequent for lichen and for sedge in 2010 and for sedge and open water in 2019.

Potts model regularization with spatial smoothing weight $\beta_0 = 1.2$ and temporal smoothing weight $\beta_1 = 3$ converged within the set limit of 30 iterations and achieved change detection accuracies of 75%–79% per image pair, an improvement of 7–12% relative to the baseline RF classification. This resulted in final overall accuracies of over 90% in each year, an improvement of 2–13% relative to the baseline RF classification (Table 2). MCCs improved substantially to 0.66 (2010–2015), 0.45 (2015–2019) and 0.66 (2010–2019). In particular, false positives in change detection, as evident from the FDR, were reduced substantially from 58% to 25% over the period 2010–2019 with Potts model

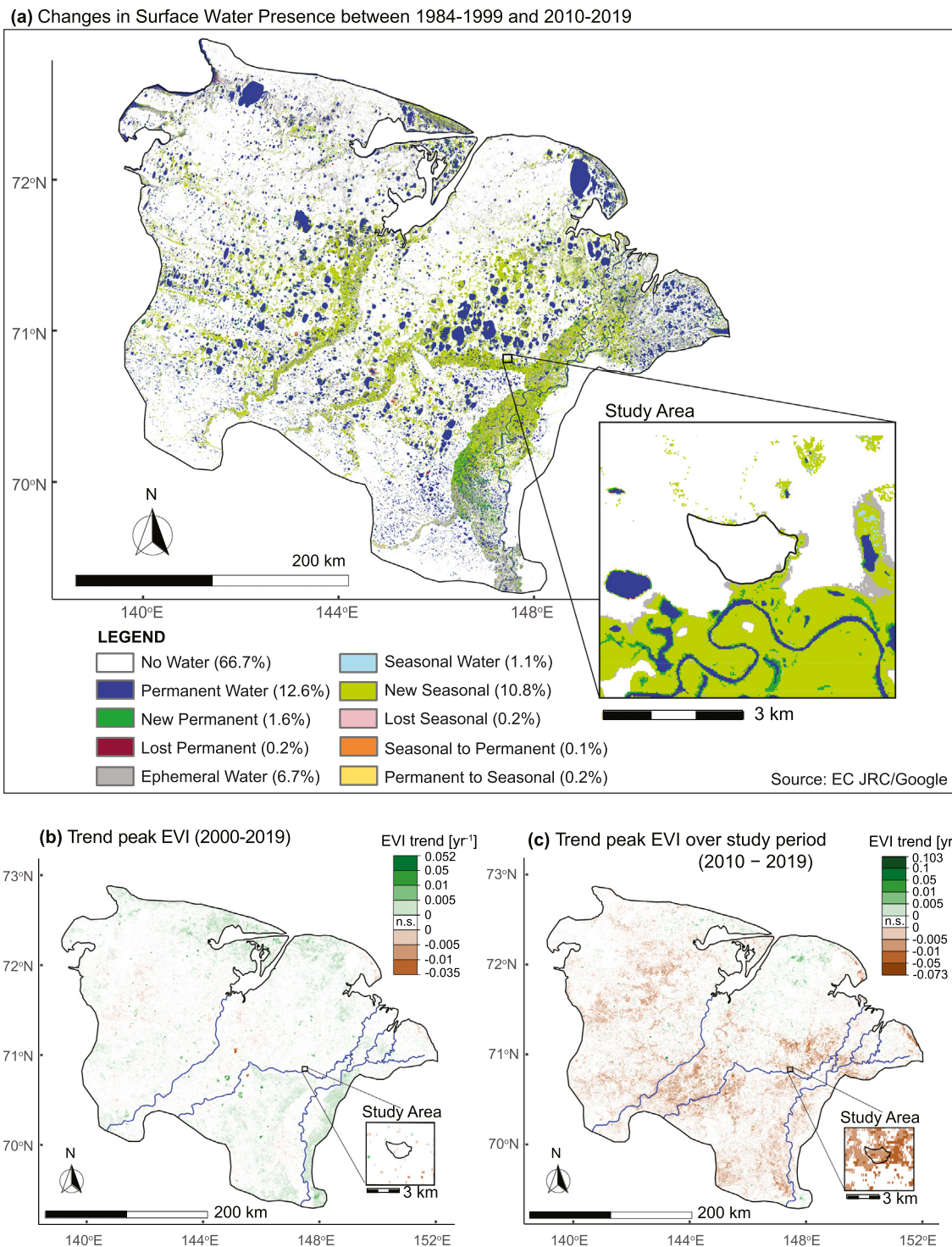


Fig. 3. Dynamics of MODIS peak growing season Enhanced Vegetation Index and surface water presence in the Indigirka Lowlands. (a) Surface water transitions between the periods 1984–1999 and 2000–2019. Numbers in legend indicate the percentage of the total area of the Indigirka Lowlands subject to that particular transition. GSWM data retrieved from <https://global-surface-water.appspot.com/map>, accessed 04-09-2020. (b) Trend in MODIS maximum growing season EVI over the MODIS observation period (2000–2019) (c) Trend in MODIS maximum growing season EVI over the high resolution land cover change analysis period (2010–2019). Larger versions of maps a–c are available in Figs. S23–S25.

regularization. This indicates that the baseline RF classification likely substantially overestimates change, confirmed by the generally higher net changes evident from the baseline classification (Table 2). Further increase of the spatial and temporal smoothing weights did not improve change detection or MCC or change detection accuracy anymore (Tables S8–S10, Figs. S16–S18). All accuracies, MCCs, convergences and other assessment criteria are visualized as heatmaps per unique combination of β_0 and β_1 in the Supplementary material, Figs. S4–

S18. All results shown hereafter are for a Potts model classification with $\beta_0 = 1.2$ and $\beta_1 = 3$.

3.3. Final classification

Final classifications in Fig. 4 showed several larger areas of stable tussock vegetation, especially on slightly elevated pingos, levees of small streams and edges of the lakebed. Two larger zones of sedge

Table 2

Classification and change detection accuracy for baseline RF and Potts model classification. The overall classification accuracy is determined for each image separately using the class labels of the test data. The change detection accuracy is determined from class labels of the validation data for each combination of two images. Net predicted change in area per class is given for both the baseline RF classification and RF + Potts model classification.

	Baseline RF classification	RF + Potts model classification
Overall classification accuracy		
Overall accuracy 2010	78%	91%
Overall accuracy 2015	91%	93%
Overall accuracy 2019	82%	91%
Change detection accuracy		
Change detection accuracy 2010–2015	69%	79%
Change detection accuracy 2015–2019	69%	76%
Change detection accuracy 2010–2019	63%	75%
Net predicted changes in land cover classes		
Net change area shrubs	−16%	−11%
Net change area tussock	−18%	−16%
Net change area lichen	−11%	−6%
Net change area open water	+34%	+49%
Net change area sedge	+19%	+11%
Net change area sphagnum	+29%	+22%

dominated vegetation were identified at the left and top right of the study area. In the center of the alas, patches of aquatic species (sedge and *Sphagnum*) as well as open water increased at the expense of shrub, tussock and lichen vegetation. *Sphagnum* showed the most pronounced expansion. Confusion matrices for classified data and test data indicated that after implementation of the Potts model with the selected parameters, most land cover classes achieved user's and

producer's accuracies of >80% (Table 2). Lichen remained relatively poorly separable from shrub and tussock, potentially explained by the overlap in species composition between these three classes (Table 1). In the 2019 image, open water was frequently misclassified as sedge, despite high separability of open water and sedge in the other images. This indicates year-to-year variability in class separability, potentially related to hydrological conditions (the early summer of 2019 was relatively dry and warm, Fig. S26).

3.4. Observed land cover change

Comparison of the total area of each class in the three images indicated that shrub and tussock vegetation decreased whereas open water, sedge and *Sphagnum* increased (Fig. 5), to an extent that the dominant class changed from shrub to *Sphagnum* by 2019. *Sphagnum* increased consistently, whereas open water and sedge increased mostly between 2010 and 2015, potentially related to the earlier date (early July) of the 2015 image compared to 2010 and 2019 (early August). Tussock vegetation showed a larger percent decline than shrubs and lichen, although similar to shrub in terms of total area affected (Fig. S19).

In terms of total area affected, the most prominent transitions were from shrub to tussock, shrub to sedge, tussock to shrub, tussock to sedge, tussock to *Sphagnum* and sedge to *Sphagnum*. In addition, open water had a high transition rate to sedge, and lichen had a high transition rate to tussock, although these changes amounted to a small net area (Fig. S19). Such transitions from open water to sedge to *Sphagnum* were also evident in the validation sites (Fig. S21), and the validation sites displayed a similar tendency of shrub decline and increase of sedge and *Sphagnum* (Fig. S20). Of all areas transitioning to open water between 2010 and 2019, 74% formed in shrub vegetation, 13% in sedge vegetation and 8% in tussock, indicating that dwarf shrub

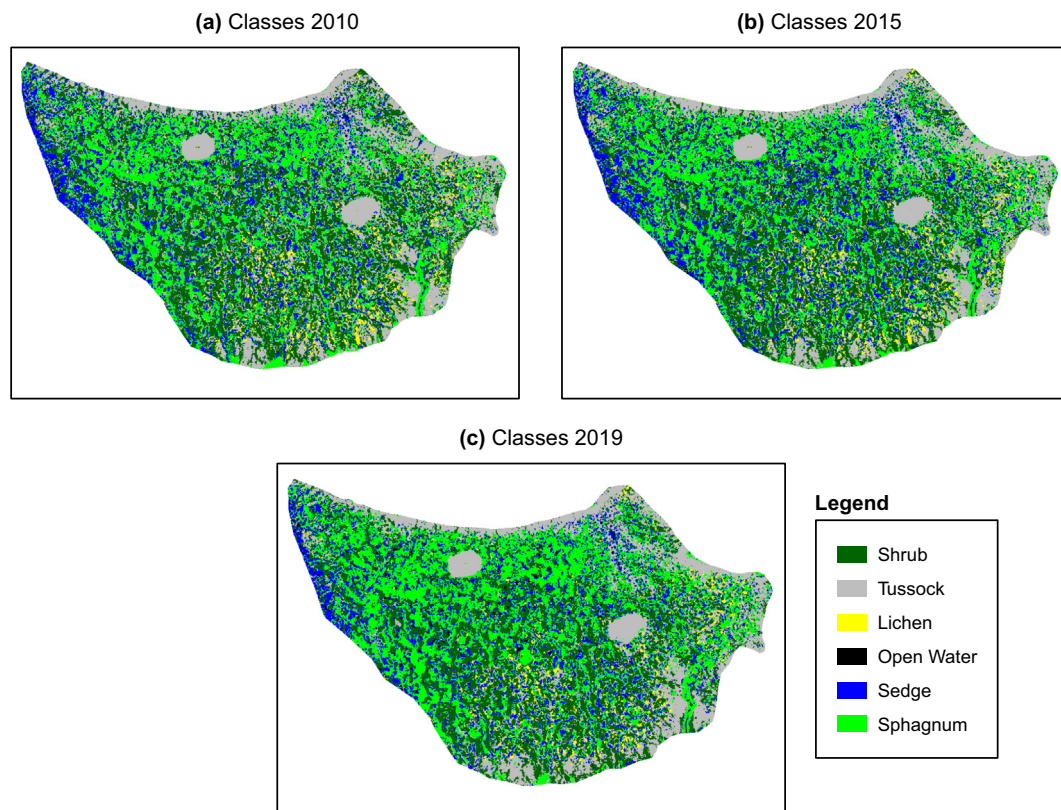


Fig. 4. Classified images using optimized weights for the Potts model. A substantial expansion of *Sphagnum* was visible, especially between 2015 (b) and 2019 (c). Higher elevation areas (edges of the alas, pingos) feature stable homogeneous tussock vegetation. The round tussock areas in the middle of the study area are pingos.

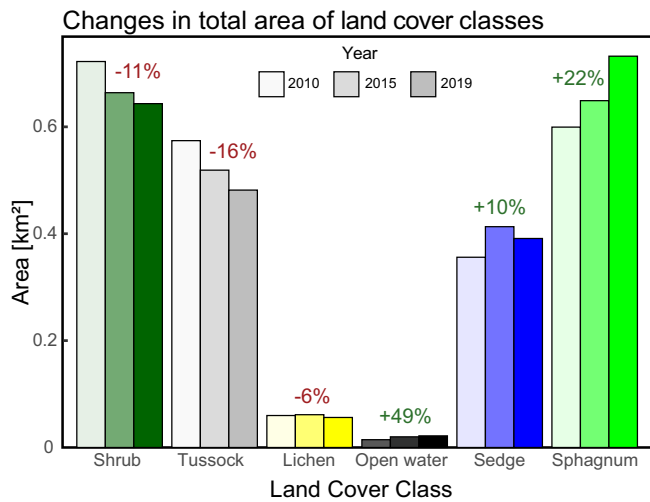


Fig. 5. Total area of each land cover class in each year for the selected Potts model classification. Numbers above bars represent change in total area over 2010–2019 relative to the total area in 2010.

vegetation in this area may be especially prone to formation of open water features.

3.5. Transition probabilities

Fig. 6 shows that transition probabilities were similar across the different time periods. Shrubs, sedge and *Sphagnum* were relatively stable classes, whereas tussock, lichen and open water showed a higher probability of transitioning to another class. The transition from open water to sedge was most prominent, with a probability of 45% over 2010–2019. Shrub and tussock also showed high transition probabilities to sedge, whereas lichen showed a high probability of transitioning to tussock. Sedge and tussock tended to transition to *Sphagnum*, whereas *Sphagnum* is a relatively stable class. Tussock had structurally high transition probabilities, except to and from open water. For 2015–2019 we found a lower probability of open water transitioning to sedge and higher probability of sedge transitioning to *Sphagnum* than for 2010–2015.

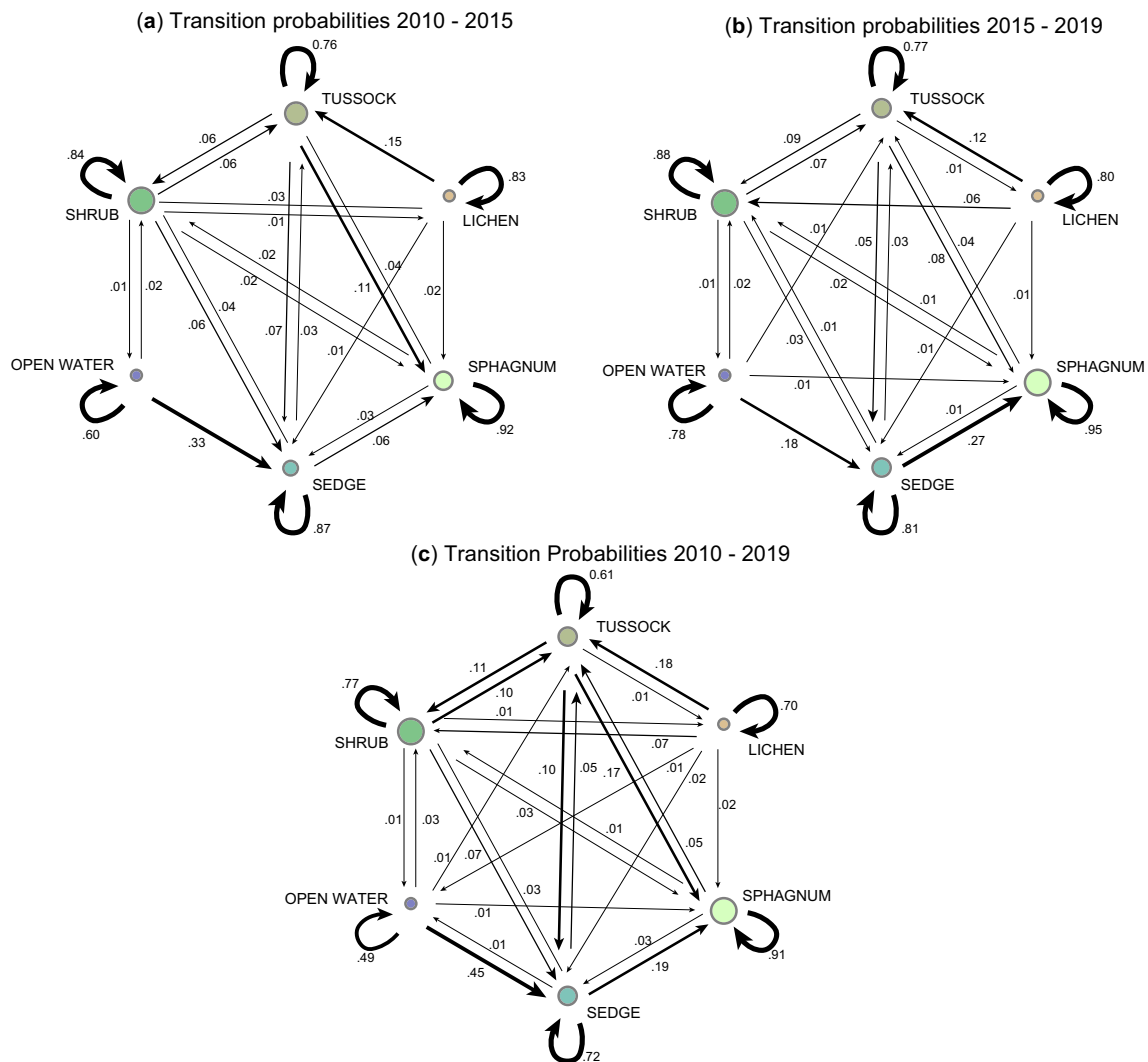


Fig. 6. Markov Chain diagrams for observed transition probabilities (0–1). Separate diagrams were generated for 2010–2015 (a), 2015–2019 (b) and 2010–2019 (c). The sizes of the circles representing each land cover class are proportional to the total area of that class. The thickness of arrows is proportional to the transition probability they represent (i.e. from one class to another). Probabilities < 0.01 are not shown.

4. Discussion

4.1. Regional trends in vegetation greening and surface water dynamics

4.1.1. Dynamics of surface water and vegetation greenness in the Indigirka Lowlands

The Landsat-derived GSWM (Pekel et al., 2016) shows large increases in the extent of permanent surface water and particularly in the extent of seasonal surface water. The floodplains of major rivers were identified as hotspots of surface water increase and showed local browning, particularly in the taiga zone along the Indigirka south of the study site (Fig. 3b–c). This may be (partially) explained by recent flood events after years with anomalously high snowmelt (Fig. S26d), resulting in detrimental effects on local vegetation (Tei et al., 2020). 2017 in particular showed extensive flooding (Tei et al., 2020) and record low regional EVI (Fig. S26e). Shkolnik et al. (2018) predicted a 2–5% increase in annual flooded area for Siberian rivers for the coming decades, with increases up to 10% in the Indigirka Lowlands. This suggests a continuation of the observed wetting trend and associated browning events observed in floodplains, with potential implications for local ecosystems and their carbon balance.

Trends in MODIS EVI indicate that greening and browning dynamics vary over space and time in the Indigirka Lowlands. Recent browning was common in floodplains and in alas terrain north of the rivers Berelekh and Khroma, while greening was more commonly observed in the coastal tundra areas and on inter-alas terrain (sensu Fedorov et al., 2018) and mountainous terrain along the floodplains of the Indigirka (Figs. 3b, 1). This hints at a divergent development of browning in lowland terrain vs. greening in upland and coastal terrain. Individual alases and thaw lake margins also show particularly pronounced changes in opposing direction, often in concert with lake expansion or drainage (Figs. 3 & S23–S24). This suggests an important role of lake hydrology in local greening dynamics, as observed earlier in coastal Alaska and in the Lena delta. Here recently drained lakes showed rapid increases in biomass and NDVI (Nitze and Grosse, 2016; Regmi et al., 2012; Zona et al., 2010), whereas browning was observed on wetting terrain such as margins of expanding thaw lakes, eroding coasts and areas affected by ice-wedge degradation (Nitze and Grosse, 2016; Raynolds and Walker, 2016; Raynolds et al., 2014). Such events may also be a direct result of terrain wetting rather than an indication of vegetation changes, as vegetation indices based on infrared reflectance are sensitive to water (Goswami et al., 2011; Lin et al., 2012; Myers-Smith et al., 2020; Raynolds and Walker, 2016).

Temporal dynamics of EVI across the Indigirka Lowlands suggest a trend break, with intensified local browning and high year-to-year variability in EVI after 2010 (Figs. 3b–c, S26e). Similar trend breaks and increased variability are observed in other Arctic regions, as climate extremes and other browning causes increase in frequency (Frost et al., 2020; Phoenix and Bjerke, 2016). Accordingly, increased variability in EVI and intensified browning in the Indigirka Lowlands was accompanied by a period with high variability in weather conditions, including extreme summer precipitation and snow height and spring heatwaves (Fig. S26). Increases in height and duration of snow cover in particular may have contributed to browning by delaying the onset of vegetation growth (Bieniek et al., 2015; Phoenix and Bjerke, 2016), potentially amplified by subsequent flooding (Tei et al., 2020) or thermokarst activity (Lara et al., 2018; Phoenix and Bjerke, 2016). Observed land cover changes in the study area support this potential explanation (Section 4.1.2).

4.1.2. Comparison of VHR land cover change and MODIS derived trends

Analysis of MODIS-derived Enhanced Vegetation Index indicated that our study area is representative for the Indigirka Lowlands in terms of range and dynamics of vegetation greenness but shows relatively strong browning in the past decade (Figs. 3c, S26e). Relating large scale trends in EVI to local vegetation processes remains

challenging, due to mismatches between the spatial scale of satellite data and small-scale vegetation patterns and confounding influences such as local hydrological dynamics (Myers-Smith et al., 2020). Despite the small spatial scale on which changes in plant functional type were expressed (Fig. 4), observed land cover change (Fig. 5) would be consistent with the observed browning trend. A decline in shrub cover was evident from high resolution change analysis, which is generally strongly related to spectral indices of vegetation greenness (Epstein et al., 2013; Forbes et al., 2010; Myers-Smith et al., 2015; Raynolds and Walker, 2016; Tape et al., 2006). Additionally, local small-scale wetting may have reduced EVI, both directly (Goswami et al., 2011; Lin et al., 2012; Myers-Smith et al., 2020; Raynolds and Walker, 2016) and through shrub mortality and shifts towards aquatic vegetation types upon inundation (Magnússon et al., 2020; Nauta et al., 2015). Alternative potential browning causes include event-based disturbances such as outbreaks of pathogens, increased herbivory, coastal erosion, salt inundation, structural changes to surface hydrology and fires (Bjerke et al., 2017; Myers-Smith et al., 2020; Phoenix and Bjerke, 2016). Lastly, browning can be related to gradual changes such as a reversal of greening causes and gradual deterioration of growing conditions (Bieniek et al., 2015; Myers-Smith et al., 2020; Phoenix and Bjerke, 2016). As EVI decreases in the study area were fairly consistent between 2010 and 2019 despite variability in weather conditions (Fig. S26e) and no obvious alternative browning mechanisms (e.g. observed fires, pathogen outbreaks or increased herbivory) were observed during the study period, wetting and associated land cover changes seem a likely explanation of observed recent browning. This raises the question whether the processes observed in the study area (small-scale thermokarst, shrub decline and transition towards wetter vegetation types) may also have contributed to larger scale intensified browning in the Indigirka Lowlands over the past decade (Fig. 3c).

Although the GSWM confirmed widespread surface wetting throughout the Indigirka Lowlands, it indicated practically no occurrence of permanent or seasonal surface water in the study area (Fig. 3a), despite the pronounced increase in open water evident from VHR images (Fig. 5). Magnússon et al. (2020) found that thaw ponds in the study area are generally very small (<100 m²) and show rapid terrestrialization. Other manifestations of thermokarst (ice-wedge degradation, expansion of diffuse drainage gullies) were also observed on much smaller spatial scales (Fig. 7b & d) than the resolution of the GSWM. Underdetection of abundant smaller ponds in thermokarst ecosystems is a known phenomenon (Grosse et al., 2008; Muster et al., 2013), which implies that surface water expansion in the Indigirka Lowlands may be larger than Landsat-derived GSWM suggests. Multi-scale analysis of vegetation greenness and surface water presence in thermokarst ecosystems, e.g. using WorldView, Landsat/Sentinel and MODIS data, is a promising direction for further research. Our results suggest that moderate to coarse resolution analysis of changes in surface spectral properties do not accurately reflect the effects of abundant small-scale thermokarst processes on shorter timescales and highlight the importance of high-resolution data for early detection and monitoring of these potentially influential phenomena.

4.2. Identified land cover change trajectories and implications for Arctic vegetation dynamics

4.2.1. Abrupt permafrost thaw as driver of shrub decline?

We found a decrease in the total area of shrubs, which is in contrast with the panarctic trend of shrub expansion. Formation and expansion of water bodies predominantly took place in shrub vegetation. Spatially, open water expansion was mostly expressed as formation of small, isolated (<100 m²) water bodies in shrub patches (see Fig. 7c, Video S1) and expansion of open water and sedge area into the edges of shrub patches (Fig. 7a–b, Video S1), often along the margins of diffuse drainage lines. As a result, most shrub patches in our study area diminished in size (Fig. 4). Shrubs patches in the study area show a relative

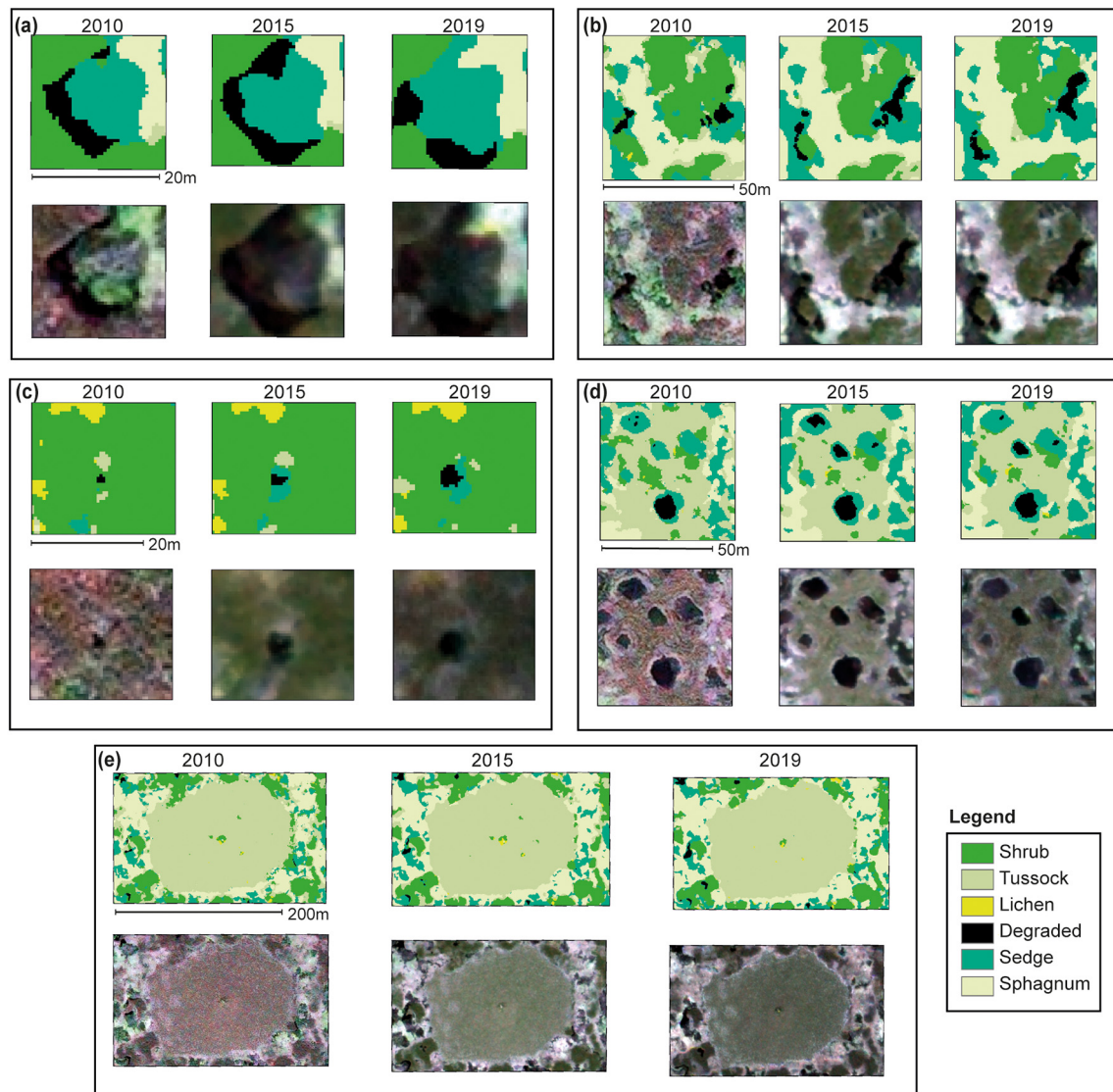


Fig. 7. Snapshots of typical vegetation change phenomena. For each panel, the top row images contain classified vegetation maps and the bottom row are pan-sharpened, true color composites (red, green and blue band) of top-of-atmosphere reflectance values (GeoEye © MAXAR, 2019, Worldview © MAXAR, 2019). (a) Edges of shrub patches tend to subside, especially along diffuse drainage lines. These subsided areas are colonized by sedges and in turn by Sphagnum carpets. (b) Same as (a), over a larger area. Sphagnum expands into previously sedge dominated areas. (c) Within shrub patches, small thaw ponds may appear. (d) Polygonal tundra appears relatively stable, although the relative amounts of sedge and open water in low center polygons seem to vary. Also, some variation in the relative amount of shrub and tussock is evident, without very visible changes in the satellite images. (e) A small, few meters high pingo, which shows stable tussock vegetation. In the bottom left, a thaw pond appears in a shrub patch. Video S1 contains a dynamic visualization of vegetation change and permafrost dynamics. (For interpretation of the references to color in this figure legend, the reader is referred to the web version of this article.)

enrichment in near-surface (top 0–20 cm of permafrost) ground ice content (Wang et al., 2019), making abrupt thaw due to loss of ground ice a likely explanation for the observed expansion of open water at the expense of shrub patches. Abrupt thaw occurs when excess ground ice is exposed to above zero temperatures due to a deepening of the active layer and melts, causing subsidence of the soil surface (Jorgenson et al., 2006; Olefeldt et al., 2016; Schuur et al., 2015) and pond formation in poorly drained, flat terrain (Nauta et al., 2015). The resulting net area displaying a transition from shrub to open water over nine years was small compared to that of other transitions (Fig. S19), but transitions from shrub to water were relatively accurately classified and somewhat underdetected (Tables S11–S13). This suggests that surface water expansion in shrub patches may be more pronounced than what is evident from our final classification. Transition of shrub vegetation to open water and sedge vegetation along the margins of diffuse drainage lines likely also represents degradation of permafrost as a result of advective heat transfer from seasonal water flow. Osterkamp et al. (2009)

observed similar expansion of thermokarst features (thermokarst gullies and thermokarst pits) along diffuse water tracks in tussock-shrub tundra in interior Alaska. Our results indicate that formation and expansion of small water bodies, likely as a result of small-scale permafrost degradation, can contribute to local shrub decline and thereby potentially contributed to recent browning observed in this site. This corroborates the importance of high spatial resolution data in the context of Arctic shrub dynamics to identify such mechanisms.

4.2.2. Aquatic succession

Analysis of transition probabilities identified a distinct change trajectory from open water to sedge to Sphagnum. Within the 9-year time span of our satellite images, 45% of open water transitioned to sedge dominated vegetation and 19% of sedge dominated areas transitioned to Sphagnum (Fig. 6). Such a succession mechanism from open water to sedges to Sphagnum confirms earlier findings of vegetation succession in thermokarst features (Jorgenson et al., 2015; Jorgenson et al.,

2010; Kanevskiy et al., 2017; Magnússon et al., 2020) and development of thermokarst bogs in boreal ecosystems (Kuhry et al., 1993; Myers-Smith et al., 2008; Payette et al., 2004; Robinson and Moore, 2000; Turetsky et al., 2007). In our study site, Magnússon et al. (2020) found that colonization of thermokarst features by sedges and *Sphagnum* mosses may occur on subdecadal to decadal timescales. Transitions from open water to sedge and from sedge to *Sphagnum* were also very pronounced in the validation data in both time intervals (Fig. S21) and relatively accurately detected (Tables S11–S13), lending further credibility to this observed trajectory. Our results suggest a succession towards bog vegetation following ponding, although the 9-year observation period likely mostly captures the rapid (aquatic) succession processes. Potential transitions towards climax vegetation, such as dwarf shrubs or tussock sedges, may require longer monitoring periods to be accurately quantified.

4.2.3. Increase in area of wetland species

Apart from aquatic successions, land cover change analysis demonstrated frequent transitions from tussock vegetation to sedge and *Sphagnum*, from lichen vegetation to tussock and from shrub vegetation to sedge or tussock (Figs. 6, S19). The former implies an expansion of wetland species, whereas the latter implies an expansion of graminoids into lichen and shrub dominated areas. This could be explained by gradual increases in active layer thickness and surface wetting. Sedges and *Sphagnum* are associated with wetter microsites (Iturrate-García et al., 2016), and graminoids can profit from nutrient release at the thaw front in mixed vegetation tundra plots whereas shrubs acquire nutrients from upper soil layers (Wang et al., 2018).

Tussock vegetation showed relatively poor spectral separability in most years (Figs. S1–S3), which may be explained by the inherently mixed nature of tussock vegetation found in this ecosystem (i.e. it contains graminoids as well as shrub and *Sphagnum* species, see Table 1). It may therefore both be more prone to false positives in change detection and more prone to gradual changes in relative species abundance. The tussock sites in the validation set mostly did not display vegetation change in reality, complicating the accuracy assessment of observed changes to and from tussock. The slow growth rate of tussock sedges (McGraw and Chapin III, 1989) makes a complete transition towards tussock sedge dominated vegetation unlikely on the observed time-scale. As such, transitions to tussock may represent gradual transitions towards a more mixed species composition. Class transitions related to gradual changes in dominant vegetation species often occur in both directions (Gómez et al., 2016), which is also evident in our site (Fig. 6). It is possible that gradual changes in the relative abundance of different species are more common than rapid, most likely disturbance-driven successions (Section 4.2.1), although these cannot be quantified with certainty with a 9-year observation period. Extended monitoring supported by repeated vegetation inventories is recommended.

4.2.4. Inter-annual and seasonal variability in land cover

The area of open water in alases can be highly variable (Desyatkin et al., 2014) and is driven both by precipitation (Desyatkin et al., 2014; Fedorov et al., 2014) and melting of local ground ice (Fedorov et al., 2014). High amounts of precipitation may enhance ponding (Nauta et al., 2015) and promote further permafrost degradation through enhanced thermal conductivity in wet soils (Hinkel et al., 2001; Jorgenson et al., 2010). The anomalously high summer precipitation in 2011 (Fig. S26c) may have contributed to the relatively large increase in open water area between 2010 and 2015. The smaller increase in open water between 2015 and 2019 may be explained by exceptionally warm conditions in the early summer of 2019 (Fig. S26a), causing open water features to fall dry and manifest as patches of wet, bare ground (Magnússon & Heijmans, pers. obs.). Accordingly, confusion matrices indicate underestimation of the area of open water in 2019 (Tables S7, S13). Similarly, the area of open water may be highest during

the early summer period and decrease gradually due to evaporative loss (Jones et al., 2009), which may have contributed to the pronounced increase in open water between 2010 and 2015 (the image for 2015 was taken in July, whereas the images for 2010 and 2019 were taken in August). It is striking that despite the later acquisition date, summer drought in 2018 and early 2019 (Fig. S26a–c), open water area still increased from 2015 to 2019 (Fig. 5). This suggests a net trend of abrupt permafrost degradation, rather than influence of hydrological variability.

We found better baseline classification accuracy (Table S6) and class separability (Figs. S1–S3) for the early summer 2015 image than for the late summer 2010 and 2019 images. This could be explained by differences in the temporal development of biomass of different vegetation types, affecting their spectral separability. For instance, Wang et al. (2016) found a difference in the timing of peak biomass between graminoids and dwarf shrubs in this site. Accordingly, spectral separability between shrub and sedge differed between the early season image and late season images (Figs. S1–S3, Tables S3–S5). In addition, the spectral appearance of vegetation changes naturally over the season, for instance through discoloration of leaf material over the season or changes in soil moisture. The classification accuracy of the 2015 image also improved least with spatiotemporal regularization, suggesting that regularization may be particularly helpful in cases where class spectral separability differs seasonally among images.

4.2.5. Microtopographical controls on land cover change

In comparison to shrub vegetation, very little formation of open water features was observed in tussock vegetation (Fig. S19), despite the roughly equal area of tussock and shrub. In contrast, widespread thermokarst has been reported in other tussock sedge ecosystems (Jorgenson et al., 2010; Osterkamp et al., 2009). In our study area, tussock vegetation was primarily found on slightly elevated or sloping terrain such as pingos, polygon rims, levees of small rivers and slightly elevated edges of the lakebed. Such areas showed few class transitions (Figs. 4 & 7d–e). Microtopographical gradients may promote drainage and decrease accumulation of water and ice (Wang et al., 2019) in the soil profile at higher elevation. In contrast, water accumulation in ice rich shrub patches in poorly drained lower areas and along the margins of diffuse drainage lines may result in soil subsidence and ponding as a result of heat transport and increased thermal conductivity (Iijima et al., 2010; Jorgenson et al., 2015; Nauta et al., 2015). This provides a likely explanation for the formation and expansion of open water in shrub patches (Fig. 4, in detail in Fig. 7a–c). A tight association between vegetation composition and dynamics and microtopography is confirmed by earlier studies (Anderson et al., 2019; Iturrate-García et al., 2016; Siewert et al., 2015).

4.3. Implications of identified land cover change for the lowland tundra ecosystem

The changes in vegetation composition we identified imply net trends of terrain wetting and permafrost degradation, with implications for greenhouse emissions. In Arctic ecosystems, *Betula nana* and to some extent *Eriophorum vaginatum* are associated with drier, upland microsites (De Groot et al., 1997; McGraw and Chapin III, 1989; Walker et al., 1989; Walker et al., 1994; Wein, 1973). In contrast, the main aquatic sedge and *Sphagnum* species in our study area (*Eriophorum angustifolium*, *Sphagnum obtusum* and *Sphagnum squarrosum*) are associated with distinctly wet to waterlogged habitats (Daniels and Eddy, 1990; Iturrate-García et al., 2016; Phillips, 1954). Hence, observed decreases in shrub, tussock and lichen versus increases in open water, aquatic sedges and *Sphagnum* strongly suggest a wetting trend.

These observed vegetation changes and related changes in terrain wetness go hand in hand with permafrost degradation. Increases in soil moisture and surface water expansion can promote permafrost

degradation through increased heat conductivity (Iijima et al., 2010; Jorgenson et al., 2015; Jorgenson et al., 2010). Formation of open water features in elevated shrub patches strongly suggests the occurrence of abrupt permafrost thaw. In this ecosystem in particular, aquatic sedge and *Sphagnum* vegetation are associated with deeper thaw depths than shrub and tussock vegetation (Magnússon et al., 2020; Van Huissteden et al., 2005). In addition, observed changes in vegetation cover may affect the tundra surface energy balance (Loranty et al., 2018a). The relatively low albedo of shrubs compared to graminoids has for instance been suggested to lead to accelerated thaw upon shrub expansion (Bonfils et al., 2012), whereas *Sphagnum* moss may have a relatively high albedo (Juszkowski et al., 2017), especially in summer. Both dwarf shrubs and their associated moss understory (Blok et al., 2011a; Blok et al., 2010) and *Sphagnum* mosses (Seppälä, 1988; Soudzilovskaia et al., 2013) can provide a direct insulating effect to the permafrost, especially when dry (Seppälä, 1988). In this ecosystem thaw depths are generally larger under *Sphagnum* carpets than under dwarf shrub dominated vegetation (Magnússon et al., 2020; Van Huissteden et al., 2005), indicating that the observed vegetation changes (Fig. 5) are likely associated with a net deepening of the active layer. Expansion of *Sphagnum* in previously waterlogged or sedge-dominated sites indicates potential for permafrost recovery (Magnússon et al., 2020).

Degradation of permafrost results in exposure of previously frozen soil organic carbon to microbial decomposition and potential release of greenhouse gases. This is anticipated to further increase climate warming, especially in cases where surface wetting favors anaerobic decomposition into methane (Meredith et al., 2019; Schuur et al., 2015). The observed increase in area of open water and wetland species and shrub decline thereby also implies an increase in methane emissions (Nauta et al., 2015; Van Huissteden et al., 2005). In contrast, accumulation of peat in thermokarst areas can facilitate storage of large amounts of carbon, especially in *Sphagnum* bogs (Gao and Couwenberg, 2015; Myers-Smith et al., 2008; Robinson and Moore, 2000; Siewert et al., 2015). In addition, *Sphagnum* growth may directly suppress methane emissions (Parmentier et al., 2011; Sundh et al., 1995; Van Huissteden et al., 2005). This implies an eventual increase in carbon sequestration through peat accumulation, which may partially mitigate high initial emissions in thermokarst wetlands (Turetsky et al., 2020). To assess resulting net changes in the greenhouse gas balance of this ecosystem, a systematic survey of greenhouse gas fluxes associated with different vegetation classes is necessary.

4.4. Recommendations for future monitoring of Arctic vegetation change

4.4.1. Use of spatiotemporal regularization to mitigate satellite image inconsistency

Satellite data consistency in terms of seasonal timing and sensor properties is an important remaining challenge in remote sensing of Arctic vegetation change (Beamish et al., 2020). We found that MRF techniques such as the Potts model can substantially improve the quantification of vegetation change in VHR satellite data from different sensors and phenological stages. Repeated field photography proved useful in the optimization of change detection. We achieved single-image accuracies of over 90%, which is high compared to other studies of pixel-based classification using similar data in similar ecosystems (Morozumi et al., 2019; Siewert et al., 2015). We found that temporal smoothing had a larger influence on the accuracy of classification of individual images than spatial smoothing (Figs. S4–S9), because in reality most pixels did not show a change in land cover class. Decreasing the temporal smoothing weight led to more false positives in change detection, whereas increasing it further led to more false negatives and did not improve MCC (Tables S8–S10).

The correct land cover transition was detected in 75% of cases over the 2010–2019 period. While this is not optimal, it suggests that identified land cover changes can serve as an approximation of field-observed

changes in land cover class. This is also supported by the similarity between observed transition probabilities between the two time intervals (Fig. 6) and the similarity between transitions observed over the study area and in the validation data (Figs. S20 & S21). User's and producer's accuracies of change detection (Tables S11–S13) indicated that change detection accuracy varies among specific transitions. Unchanged areas achieve higher accuracies of change detection than changed areas. Overestimation of transitions among shrub, tussock and lichen in particular, likely due to poorer spectral separability (Figs. S1–S3, Tables S3–S5). Transitions between open water, sedge and *Sphagnum* generally achieved higher accuracies (Tables S11–S13).

4.4.2. Recommendations for further improvement of change detection accuracy

MRF may be a valuable technique to explore further in the context of Arctic vegetation change and may stimulate (re)use of existing image material. For instance, MRF-based approaches can be modified to explicitly penalize specific illogical class transitions (Wehmann and Liu, 2015), which may prove useful in cases where a priori information is available on land cover change mechanisms. Gómez et al. (2016) provide an overview of MRF applications and post-classification amendments to enhance temporal consistency in land cover change detection. In addition, other optimization methods than ICM could be applied. ICM identifies a local optimum that may theoretically differ from the global optimum. Alternative optimization techniques such as graph cuts are demonstrated to always reach a global optimum within reasonable processing times for Potts models (Ishikawa, 2003). However, we find that ICM works well in practice since classification accuracies are improved substantially and convergence was generally reached within 30 iterations (Fig. S12).

Given the tight association between vegetation composition and microtopography (Section 4.2.5) the incorporation of multi-temporal, high resolution elevation data or other non-spectral data could substantially improve land cover change detection in Arctic ecosystems (Beamish et al., 2020; Chasmer et al., 2014). Lastly, although the different temporal development in spectral properties of plant species can complicate classification (Section 4.2.4), the use of multiple images from different moments during the growing season provides complementary information that can help distinguish different vegetation types (Westergaard-Nielsen et al., 2013).

4.5. Conclusions & recommendations

To make reliable assessments of future vegetation development in the Arctic, there is an urgent need to identify underlying mechanisms of observed spatial differences in the response of Arctic vegetation to global change. During the past decade we observed a browning trend instead of greening in our Siberian lowland tundra site. This was associated with a decline of shrub and tussock dominated vegetation, which was rapidly replaced by open water, aquatic sedges and *Sphagnum* moss. These changes likely went hand in hand with surface wetting and degradation of ice-rich permafrost, with potential consequences for the greenhouse gas balance of this ecosystem. Comparison with regional dynamics of vegetation greenness and surface water presence indicates that similar to the study site, the Indigirka Lowlands have undergone substantial expansion of surface water features. The recent browning observed for the study site was evident in large parts of the Indigirka Lowlands, although specific areas (e.g. coastal tundra and drained thaw lakes) have continued greening.

Within our relatively short study period, land cover change was expressed on small spatial scales. Expansion of small water bodies and vegetation successions were only detected using very high resolution satellite data with extensive ground truthing. Although the influence of difference in sensors and seasonal timing of the images within this short timeseries cannot be ruled out completely, land cover change detection accuracy was improved after spatiotemporal regularization

using Potts model and false detection of land cover change was reduced substantially. Such MRF-based techniques may be compelling tools for studies of Arctic vegetation change, which are often limited by low availability and consistency of image material.

Our findings provide a contrast to earlier reports of greening and shrub expansion in the Russian Arctic and raise the question why shrubs show opposing regional trends in their expansion dynamics. Our results suggest that surface wetting and abrupt permafrost thaw could be local drivers of browning and shrub decline in this poorly drained terrain. We recommend that future research continues to relate observed large-scale trends in vegetation change to regional variability in microtopography, permafrost characteristics and hydrology. Very high resolution data proved invaluable in this context.

Supplementary data to this article can be found online at <https://doi.org/10.1016/j.scitotenv.2021.146877>.

CRediT authorship contribution statement

Rúna Magnússon: conceptualization, methodology, investigation, analysis, writing, visualization.

Juul Limpens: conceptualization, supervision, investigation, writing – review & editing.

David Kleijn: conceptualization, supervision, writing – review & editing.

Ko van Huissteden: resources, writing – review & editing.

Trofim Maximov: resources, supervision, project administration.

Sylvain Lobry: methodology, writing – review & editing.

Monique Heijmans: conceptualization, resources, supervision, project administration, funding acquisition, writing – review & editing.

Declaration of competing interest

The authors declare that they have no known competing financial interests or personal relationships that could have appeared to influence the work reported in this paper.

Funding & acknowledgements

This work was funded by the Netherlands Polar Programme of the Dutch Research Council (NWO) [grant number ALWPP.2016.008]. The field campaigns supporting this work received funding from the European Union's Horizon 2020 project INTERACT [grant agreement number 730938]. The funding sources had no role in the conceptualization, execution or submission for publication of this study. Sylvain Lobry worked on this project during a post-doctoral position at the Laboratory of Geo-Information Science and Remote Sensing, Wageningen University, The Netherlands. We thank Sergey Karsanaev, Roman Petrov and Egor Starostin of the Institute for Biological Problems of the Cryolithozone of the Siberian Branch of the Russian Academy of Sciences, and Tatyana Stryukova and colleagues of the Regional Inspection of Nature Protection of the Allaihovskiy Region for logistic support. We thank Katrien Kurvers MSc for exploratory analysis on the satellite images. Data used for this study are available from the DANS EASY repository (Magnússon, 2021), except copyrighted satellite images (see Table S1).

References

Abbott, B.W., Jones, J.B., Schuur, E.A., Chapin III, F.S., Bowden, W.B., Bret-Harte, M.S., Epstein, H.E., Flannigan, M.D., Harms, T.K., Hollingsworth, T.N., 2016. Biomass offsets little or none of permafrost carbon release from soils, streams, and wildfire: an expert assessment. *Environ. Res. Lett.* 11, 034014.

Anderson, J.E., Douglas, T.A., Barbato, R.A., Saari, S., Edwards, J.D., Jones, R.M., 2019. Linking vegetation cover and seasonal thaw depths in interior Alaska permafrost terrains using remote sensing. *Remote Sens. Environ.* 233, 111363.

Aspinall, R.J., Hill, M., 1997. Land cover change: a method for assessing the reliability of land cover changes measured from remotely-sensed data. *IGARSS'97. 1997 IEEE International Geoscience and Remote Sensing Symposium Proceedings. Remote Sensing-A Scientific Vision for Sustainable Development. IEEE*, pp. 269–271.

Beamish, A., Reynolds, M.K., Epstein, H., Frost, G.V., Macander, M.J., Bergstedt, H., Bartsch, A., Kruse, S., Miles, V., Tanis, C.M., Heim, B., Fuchs, M., Chabrilat, S., Shevtsova, I., Verdonen, M., Wagner, J., 2020. Recent trends and remaining challenges for optical remote sensing of Arctic tundra vegetation: a review and outlook. *Remote Sens. Environ.* 246, 111872.

Besag, J., 1986. On the statistical analysis of dirty pictures. *J. R. Stat. Soc. Ser. B Methodol.* 48, 259–279.

Bhatt, U.S., Walker, D.A., Reynolds, M.K., Bieniek, P.A., Epstein, H.E., Comiso, J.C., Pinzon, J.E., Tucker, C.J., Steele, M., Ermold, W., 2017. Changing seasonality of panarctic tundra vegetation in relationship to climatic variables. *Environ. Res. Lett.* 12, 055003.

Bhattacharyya, A., 1946. On a measure of divergence between two multinomial populations. *Sankhyā Indian J. Stat. (1933–1960)* 7, 401–406.

Bieniek, P.A., Bhatt, U.S., Walker, D.A., Reynolds, M.K., Comiso, J.C., Epstein, H.E., Pinzon, J.E., Tucker, C.J., Thoman, R.L., Tran, H., 2015. Climate drivers linked to changing seasonality of Alaska coastal tundra vegetation productivity. *Earth Interact.* 19, 1–29.

Bjerke, J.W., Treharne, R., Vikhamar-Schuler, D., Karlsen, S.R., Ravolainen, V., Bokhorst, S., Phoenix, G.K., Bochenek, Z., Tømmervik, H., 2017. Understanding the drivers of extensive plant damage in boreal and Arctic ecosystems: insights from field surveys in the aftermath of damage. *Sci. Total Environ.* 599, 1965–1976.

Bjorkman, A.D., Criado, M.G., Myers-Smith, I.H., Ravolainen, V., Jónsdóttir, I.S., Westergaard, K.B., Lawler, J.P., Aronsson, M., Bennett, B., Gardfjell, H., 2020. Status and trends in Arctic vegetation: evidence from experimental warming and long-term monitoring. *Ambio* 49, 678–692.

Blok, D., Heijmans, M.M., Schaepman-Strub, G., Kononov, A., Maximov, T., Berendse, F., 2010. Shrub expansion may reduce summer permafrost thaw in Siberian tundra. *Glob. Chang. Biol.* 16, 1296–1305.

Blok, D., Heijmans, M., Schaepman-Strub, G., van Ruijven, J., Parmentier, F., Maximov, T., Berendse, F., 2011a. The cooling capacity of mosses: controls on water and energy fluxes in a Siberian tundra site. *Ecosystems* 14, 1055–1065.

Blok, D., Sass-Klaassen, U., Schaepman-Strub, G., Heijmans, M., Sauren, P., Berendse, F., 2011b. What are the main climate drivers for shrub growth in Northeastern Siberian tundra? *Biogeosciences* 8, 1169–1179.

Bonfils, C., Phillips, T., Lawrence, D., Cameron-Smith, P., Riley, W., Subin, Z., 2012. On the influence of shrub height and expansion on northern high latitude climate. *Environ. Res. Lett.* 7, 015503.

Cai, S., Liu, D., Sulla-Menashe, D., Friedl, M.A., 2014. Enhancing MODIS land cover product with a spatial-temporal modeling algorithm. *Remote Sens. Environ.* 147, 243–255.

Chasmer, L., Hopkinson, C., Veness, T., Quinton, W., Baltzer, J., 2014. A decision-tree classification for low-lying complex land cover types within the zone of discontinuous permafrost. *Remote Sens. Environ.* 143, 73–84.

Chicco, D., Jurman, G., 2020. The advantages of the Matthews correlation coefficient (MCC) over F1 score and accuracy in binary classification evaluation. *BMC Genomics* 21, 6.

Congalton, R.G., 1991. A review of assessing the accuracy of classifications of remotely sensed data. *Remote Sens. Environ.* 37, 35–46.

Daniels, R.E., Eddy, A., 1990. Handbook of European Sphagna. HMSO.

Davison, A.C., Hinkley, D.V., 1997. Bootstrap Methods and Their Application. Cambridge University Press, Cambridge.

De Groot, W., Thomas, P., Wein, R.W., 1997. *Betula nana* L. and *Betula glandulosa* Michx. *J. Ecol.* 85, 241–264.

Desyatkin, A.R., Takakai, F., Hatano, R., 2014. Flood effect on CH₄ emission from the alar in Central Yakutia, East Siberia. *Soil Sci. Plant Nutrition* 60, 242–253.

Didan, K., 2015a. MOD13Q1 MODIS/Terra vegetation indices 16-day L3 global 250m SIN grid V006. NASA EOSDIS Land Processes DAAC, p. 10.

Didan, K., 2015b. MYD13Q1 MODIS/aqua vegetation indices 16-day L3 global 250m SIN grid V006. NASA EOSDIS Land Processes DAAC, p. 10.

Elmendorf, S.C., Henry, G.H., Hollister, R.D., Björk, R.G., Boulanger-Lapointe, N., Cooper, E.J., Cornelissen, J.H., Day, T.A., Dorrepaal, E., Elumeeva, T.G., 2012. Plot-scale evidence of tundra vegetation change and links to recent summer warming. *Nat. Clim. Chang.* 2, 453.

Epstein, H.E., Reynolds, M.K., Walker, D.A., Bhatt, U.S., Tucker, C.J., Pinzon, J.E., 2012. Dynamics of aboveground phytomass of the circumpolar Arctic tundra during the past three decades. *Environ. Res. Lett.* 7, 015506.

Epstein, H.E., Myers-Smith, I., Walker, D.A., 2013. Recent dynamics of arctic and sub-arctic vegetation. *Environ. Res. Lett.* 8, 015040.

ESRI, 2019. ArcGIS Desktop. Environmental Systems Research Institute, Redlands, CA.

Fedorov, A., Ivanova, R., Park, H., Hiyama, T., Iijima, Y., 2014. Recent air temperature changes in the permafrost landscapes of northeastern Eurasia. *Polar Sci.* 8, 114–128.

Fedorov, A.N., Vasilyev, N.F., Torgovkin, Y.I., Shestakova, A.A., Varlamov, S.P., Zheleznyak, M.N., Shepelev, V.V., Konstantinov, P.Y., Kalinicheva, S.S., Basharin, N.I., 2018. Permafrost-landscape map of the republic of Sakha (Yakutia) on a scale 1: 1,500,000. *Geosciences* 8, 465.

Forbes, B.C., Fauria, M.M., Zetterberg, P., 2010. Russian Arctic warming and 'greening' are closely tracked by tundra shrub willows. *Glob. Chang. Biol.* 16, 1542–1554.

Frost, G.V., Epstein, H.E., Walker, D.A., 2014. Regional and landscape-scale variability of Landsat-observed vegetation dynamics in northwest Siberian tundra. *Environ. Res. Lett.* 9, 025004.

Frost, G.V., Bhatt, U.S., Epstein, H.E., Myers-Smith, I., Phoenix, G.K., Berner, L.T., Bjerke, J.W., Forbes, B.C., Goetz, S.J., Kerby, J.T., Macander, M.J., Park, T., Reynolds, M.K., Tømmervik, H., Walker, D.A., 2020. Arctic Report Card 2020: Tundra Greenness.

Gao, Y., Couwenberg, J., 2015. Carbon accumulation in a permafrost polygon peatland: steady long-term rates in spite of shifts between dry and wet conditions. *Glob. Chang. Biol.* 21, 803–815.

Geman, S., Geman, D., 1984. Stochastic relaxation, Gibbs distributions, and the Bayesian restoration of images. *IEEE Trans. Pattern Anal. Mach. Intell.* 721–741.

- Gómez, C., White, J.C., Wulder, M.A., 2016. Optical remotely sensed time series data for land cover classification: a review. *ISPRS J. Photogramm. Remote Sens.* 116, 55–72.
- Goswami, S., Gamon, J.A., Tweedie, C.E., 2011. Surface hydrology of an arctic ecosystem: multiscale analysis of a flooding and draining experiment using spectral reflectance. *J. Geophys. Res. Biogeosci.* 116.
- Grosse, G., Romanovsky, V., Walter, K., Morgenstern, A., Lantuit, H., Zimov, S., 2008. Distribution of Thermokarst Lakes and Ponds at Three Yedoma Sites in Siberia (In).
- Hinkel, K., Paetzold, F., Nelson, F., Bockheim, J., 2001. Patterns of soil temperature and moisture in the active layer and upper permafrost at Barrow, Alaska: 1993–1999. *Glob. Planet. Chang.* 29, 293–309.
- van Huissteden, J., 2020. Thawing Permafrost: Permafrost Carbon in a Warming Arctic. Springer Nature.
- Iijima, Y., Fedorov, A.N., Park, H., Suzuki, K., Yabuki, H., Maximov, T.C., Ohata, T., 2010. Abrupt increases in soil temperatures following increased precipitation in a permafrost region, central Lena River basin, Russia. *Permafrost. Periglac. Process.* 21, 30–41.
- Ishikawa, H., 2003. Exact optimization for Markov random fields with convex priors. *IEEE Trans. Pattern Anal. Mach. Intell.* 25, 1333–1336.
- Iturrate-García, M., O'Brien, M.J., Khitun, O., Abiven, S., Niklaus, P.A., Schaeppman-Strub, G., 2016. Interactive effects between plant functional types and soil factors on tundra species diversity and community composition. *Ecol. Evol.* 6, 8126–8137.
- Iwahana, G., Takano, S., Petrov, R.E., Tei, S., Shingubara, R., Maximov, T.C., Fedorov, A.N., Desyatkin, A.R., Nikolaev, A.N., Desyatkin, R.V., 2014. Geocryological characteristics of the upper permafrost in a tundra-forest transition of the Indigirka River Valley, Russia. *Polar Sci.* 8, 96–113.
- Jones, B.M., Arp, C.D., Hinkel, K.M., Beck, R.A., Schmutz, J.A., Winston, B., 2009. Arctic lake physical processes and regimes with implications for winter water availability and management in the National Petroleum Reserve Alaska. *Environ. Manag.* 43, 1071–1084.
- Jorgenson, M., Shur, Y.L., Pullman, E.R., 2006. Abrupt increase in permafrost degradation in Arctic Alaska. *Geophys. Res. Lett.* 33.
- Jorgenson, M.T., Romanovsky, V., Harden, J., Shur, Y., O'Donnell, J., Schuur, E.A., Kanevskiy, M., Marchenko, S., 2010. Resilience and vulnerability of permafrost to climate change. *Can. J. For. Res.* 40, 1219–1236.
- Jorgenson, M.T., Kanevskiy, M., Shur, Y., Moskalenko, N., Brown, D., Wickland, K., Striegl, R., Koch, J., 2015. Role of ground ice dynamics and ecological feedbacks in recent ice wedge degradation and stabilization. *J. Geophys. Res. Earth Surf.* 120, 2280–2297.
- Juszk, I., Iturrate-García, M., Gastellu-Etchegorry, J.-P., Schaeppman, M.E., Maximov, T.C., Schaeppman-Strub, G., 2017. Drivers of shortwave radiation fluxes in Arctic tundra across scales. *Remote Sens. Environ.* 193, 86–102.
- Kanevskiy, M., Shur, Y., Jorgenson, T., Brown, D.R., Moskalenko, N., Brown, J., Walker, D.A., Raynolds, M.K., Buchhorn, M., 2017. Degradation and stabilization of ice wedges: implications for assessing risk of thermokarst in northern Alaska. *Geomorphology* 297, 20–42.
- Kuhry, P., Nicholson, B.J., Gignac, L.D., Vitt, D.H., Bayley, S.E., 1993. Development of Sphagnum-dominated peatlands in boreal continental Canada. *Can. J. Bot.* 71, 10–22.
- Lara, M.J., Nitze, I., Grosse, G., Martin, P., McGuire, A.D., 2018. Reduced arctic tundra productivity linked with landform and climate change interactions. *Sci. Rep.* 8, 2345.
- Li, B., 2017. A Clash of Plants: Vegetation Succession and Its Interaction With Permafrost Dynamics in the Arctic Lowland Tundra.
- Li, B., Heijmans, M.M., Blok, D., Wang, P., Karsanaev, S.V., Maximov, T.C., van Huissteden, J., Berendse, F., 2017. Thaw pond development and initial vegetation succession in experimental plots at a Siberian lowland tundra site. *Plant Soil* 420, 147–162.
- Lin, D., Johnson, D., Andresen, C., Tweedie, C., 2012. High spatial resolution decade-time scale land cover change at multiple locations in the Beringian Arctic (1948–2000s). *Environ. Res. Lett.* 7, 025502.
- Lorant, M.M., Abbott, B.W., Blok, D., Douglas, T.A., Epstein, H.E., Forbes, B.C., Jones, B.M., Kholodov, A.L., Kropp, H., Malhotra, A., 2018a. Reviews and syntheses: changing ecosystem influences on soil thermal regimes in northern high-latitude permafrost regions. *Biogeosciences* 15, 5287–5313.
- Lorant, M.M., Davydov, S.P., Kropp, H., Alexander, H.D., Mack, M.C., Natali, S.M., Zimov, N.S., 2018b. Vegetation indices do not capture forest cover variation in Upland Siberian larch forests. *Remote Sens.* 10 (11), 1686.
- MacLeod, R.D., Congalton, R.G., 1998. A quantitative comparison of change-detection algorithms for monitoring eelgrass from remotely sensed data. *Photogramm. Eng. Remote Sens.* 64, 207–216.
- Magnússon, R.Í., 2021. Dataset for “shrub decline and expansion of wetland vegetation revealed by very high resolution land cover change detection in the Siberian lowland tundra”. DANS EASY <https://doi.org/10.17026/dans-zke-thy4>.
- Magnússon, R.Í., Limpens, J., van Huissteden, J., Kleijn, D., Maximov, T.C., Rotbarth, R., Sass-Klaassen, U., Heijmans, M.M., 2020. Rapid vegetation succession and coupled permafrost dynamics in Arctic thaw ponds in the Siberian lowland tundra. *J. Geophys. Res. Biogeosci.* 125, e2019JG005618. <https://doi.org/10.1029/2019JG005618>.
- Martin, A.C., Jeffers, E.S., Petrokofsky, G., Myers-Smith, I., Macias-Fauria, M., 2017. Shrub growth and expansion in the Arctic tundra: an assessment of controlling factors using an evidence-based approach. *Environ. Res. Lett.* 12, 085007.
- Matthews, B.W., 1975. Comparison of the predicted and observed secondary structure of T4 phage lysozyme. *Biochim. Biophys. Acta (BBA) Protein Struct.* 405, 442–451.
- McGraw, J.B., Chapin III, F.S., 1989. Competitive ability and adaptation to fertile and infertile soils in two *Eriophorum* species. *Ecology* 70, 736–749.
- McGuire, A.D., Lawrence, D.M., Koven, C., Klein, J.S., Burke, E., Chen, G., Jafarov, E., MacDougall, A.H., Marchenko, S., Nicolovsky, D., 2018. Dependence of the evolution of carbon dynamics in the northern permafrost region on the trajectory of climate change. *Proc. Natl. Acad. Sci.* 115, 3882–3887.
- Meredith, M., Sommerkorn, M., Cassotta, S., Derksen, C., Ekaykin, A., Hollowed, A., Kofinas, G., Mackintosh, A., Melbourne-Thomas, J., Muelbert, M.M.C., Ottersen, G., Pritchard, H., Schuur, E.A.G., 2019. Polar regions. In: Pörtner, D.C.R. H.-O., Masson-Delmotte, V., Zhai, P., Tignor, M., Poloczanska, E., Mintenbeck, K., Alegría, A., Nicolai, M., Okem, A., Petzold, J., Rama, B., Weyer, N.M. (Eds.), Polar regions. In: IPCC Special Report on the Ocean and Cryosphere in a Changing Climate (In press).
- van der Molen, M., van Huissteden, J., Parmentier, F., Petrescu, A., Dolman, A., Maximov, T., Kononov, A., Karsanaev, S., Suzdalov, D., 2007. The growing season greenhouse gas balance of a continental tundra site in the Indigirka lowlands, NE Siberia. *Biogeosciences* 4, 985–1003.
- Morozumi, T., Shingubara, R., Suzuki, R., Kobayashi, H., Tei, S., Takano, S., Fan, R., Liang, M., Maximov, T., Sugimoto, A., 2019. Estimating methane emissions using vegetation mapping in the taiga-tundra boundary of a north-eastern Siberian lowland. *Tellus B Chem. Phys. Meteorol.* 71, 1581004.
- Muller, M.R., Middleton, J., 1994. A Markov model of land-use change dynamics in the Niagara Region, Ontario, Canada. *Landsc. Ecol.* 9, 151–157.
- Muster, S., Heim, B., Abnizova, A., Boike, J., 2013. Water body distributions across scales: a remote sensing based comparison of three arctic tundra wetlands. *Remote Sens.* 5, 1498–1523.
- Myers-Smith, I., Harden, J., Wilking, M., Fuller, C., McGuire, A., Chapin III, F., 2008. Wetland succession in a permafrost collapse: interactions between fire and thermokarst. *Biogeosciences* 5, 1273–1286.
- Myers-Smith, I.H., Elmendorf, S.C., Beck, P.S., Wilking, M., Hallinger, M., Blok, D., Tape, K.D., Rayback, S.A., Macias-Fauria, M., Forbes, B.C., 2015. Climate sensitivity of shrub growth across the tundra biome. *Nat. Clim. Chang.* 5, 887.
- Myers-Smith, I.H., Kerby, J.T., Phoenix, G.K., Bjerke, J.W., Epstein, H.E., Assmann, J.J., John, C., Andreu-Hayles, L., Angers-Blondin, S., Beck, P.S.A., Berner, L.T., Bhatt, U.S., Bjorkman, A.D., Blok, D., Bryn, A., Christiansen, C.T., Cornelissen, J.H.C., Cunliffe, A.M., Elmendorf, S.C., Forbes, B.C., Goetz, S.J., Hollister, R.D., de Jong, R., Lorant, M.M., Macias-Fauria, M., Maseyk, K., Normand, S., Olofsson, J., Parker, T.C., Parmentier, F.-J.W., Post, E., Schaeppman-Strub, G., Stordal, F., Sullivan, P.F., Thomas, H.J.D., Tømmervik, H., Treharne, R., Tweedie, C.E., Walker, D.A., Wilking, M., Wipf, S., 2020. Complexity revealed in the greening of the Arctic. *Nat. Clim. Chang.* 10, 106–117.
- Naito, A.T., Cairns, D.M., 2011. Relationships between Arctic shrub dynamics and topographically derived hydrologic characteristics. *Environ. Res. Lett.* 6, 045506.
- Nauta, A.L., Heijmans, M.M., Blok, D., Limpens, J., Elberling, B., Gallagher, A., Li, B., Petrov, R.E., Maximov, T.C., Van Huissteden, J., 2015. Permafrost collapse after shrub removal shifts tundra ecosystem to a methane source. *Nat. Clim. Chang.* 5, 67.
- Nitzbon, J., Westermann, S., Langer, M., Martin, L.C.P., Strauss, J., Laboor, S., Boike, J., 2020. Fast response of cold ice-rich permafrost in northeast Siberia to a warming climate. *Nat. Commun.* 11, 2201.
- Nitze, I., Grosse, G., 2016. Detection of landscape dynamics in the Arctic Lena Delta with temporally dense Landsat time-series stacks. *Remote Sens. Environ.* 181, 27–41.
- Olefeldt, D., Goswami, S., Grosse, G., Hayes, D., Hugelius, G., Kuhry, P., McGuire, A.D., Romanovsky, V., Sannel, A.B.K., Schuur, E., 2016. Circumpolar distribution and carbon storage of thermokarst landscapes. *Nat. Commun.* 7, 13043.
- Osterkamp, T., Jorgenson, M., Schuur, E., Shur, Y., Kanevskiy, M., Vogel, J., Tumskey, V., 2009. Physical and ecological changes associated with warming permafrost and thermokarst in interior Alaska. *Permafrost. Periglac. Process.* 20, 235–256.
- Parmentier, F.-J.W., Huissteden, J., Kip, N., Op den Camp, H., Jetten, M., Maximov, T., Dolman, A., 2011. The Role of Endophytic Methane Oxidizing Bacteria in Submerged Sphagnum in Determining Methane Emissions of Northeastern Siberian Tundra.
- Payette, S., Delwaide, A., Caccianiga, M., Beauchemin, M., 2004. Accelerated thawing of subarctic peatland permafrost over the last 50 years. *Geophys. Res. Lett.* 31.
- Pearson, R.G., Phillips, S.J., Lorant, M.M., Beck, P.S., Damoulas, T., Knight, S.J., Goetz, S.J., 2013. Shifts in Arctic vegetation and associated feedbacks under climate change. *Nat. Clim. Chang.* 3, 673–677.
- Pekel, J.-F., Cottam, A., Gorelick, N., Belward, A.S., 2016. High-resolution mapping of global surface water and its long-term changes. *Nature* 540, 418–422.
- Phillips, M.E., 1954. *Eriophorum angustifolium* Roth. *J. Ecol.* 42, 612–622.
- Phoenix, G.K., Bjerke, J.W., 2016. Arctic greening: extreme events and trends reversing arctic greening. *Glob. Chang. Biol.* 22, 2960–2962.
- Podger, N.E., Colwell, W., Taylor, M., 2011. GeoEye-1 radiance at aperture and planetary reflectance. *GeoEye* 1–5.
- Potts, R., 1952. Some generalized order-disorder transformations. *Mathematical Proceedings of the Cambridge Philosophical Society*. Cambridge University Press, pp. 106–109.
- R Development Core Team, 2019. R: A Language and Environment for Statistical Computing. R Foundation for Statistical Computing, Vienna, Austria.
- Raynolds, M.K., Walker, D.A., 2016. Increased wetness confounds Landsat-derived NDVI trends in the central Alaska North Slope region, 1985–2011. *Environ. Res. Lett.* 11, 085004.
- Raynolds, M.K., Walker, D.A., Ambrosius, K.J., Brown, J., Everett, K.R., Kanevskiy, M., Kofinas, G.P., Romanovsky, V.E., Shur, Y., Webber, P.J., 2014. Cumulative geocological effects of 62 years of infrastructure and climate change in ice-rich permafrost landscapes, Prudhoe Bay Oilfield, Alaska. *Glob. Chang. Biol.* 20, 1211–1224.
- Raynolds, M.K., Walker, D.A., Balser, A., Bay, C., Campbell, M., Cherosov, M.M., Daniëls, F.J., Eidesen, P.B., Ermokhina, K.A., Frost, G.V., 2019. A raster version of the Circumpolar Arctic Vegetation Map (CAVM). *Remote Sens. Environ.* 232, 111297.
- Regmi, P., Grosse, G., Jones, M., Jones, B., Anthony, K., 2012. Characterizing post-drainage succession in thermokarst lake basins on the Seward Peninsula, Alaska with TerraSAR-X backscatter and Landsat-based NDVI data. *Remote Sens.* 4, 3741–3765.
- Robinson, S.D., Moore, T., 2000. The influence of permafrost and fire upon carbon accumulation in high boreal peatlands, Northwest Territories, Canada. *Arct. Antarct. Alp. Res.* 32, 155–166.
- Schuur, E.A., McGuire, A.D., Schädel, C., Grosse, G., Harden, J., Hayes, D.J., Hugelius, G., Koven, C., Kuhry, P., Lawrence, D.M., 2015. Climate change and the permafrost carbon feedback. *Nature* 520, 171.

- Seppälä, M., 1988. Palsa and related forms. In: Clark, W.:M.J. (Ed.), *Advances in Periglacial Geomorphology*. John Wiley & Sons.
- Serra, P., Pons, X., Saurí, D., 2003. Post-classification change detection with data from different sensors: some accuracy considerations. *Int. J. Remote Sens.* 24, 3311–3340.
- Shkolnik, I., Pavlova, T., Efimov, S., Zhuravlev, S., 2018. Future changes in peak river flows across northern Eurasia as inferred from an ensemble of regional climate projections under the IPCC RCP8.5 scenario. *Clim. Dyn.* 50, 215–230.
- Siewert, M.B., Hanisch, J., Weiss, N., Kuhry, P., Maximov, T.C., Hugelius, G., 2015. Comparing carbon storage of Siberian tundra and taiga permafrost ecosystems at very high spatial resolution. *J. Geophys. Res. Biogeosci.* 120, 1973–1994.
- Singh, A., 1989. Review article digital change detection techniques using remotely-sensed data. *Int. J. Remote Sens.* 10, 989–1003.
- Solberg, A.H.S., Taxt, T., Jain, A.K., 1996. A Markov random field model for classification of multisource satellite imagery. *IEEE Trans. Geosci. Remote Sens.* 34, 100–113.
- Song, C., Woodcock, C.E., Seto, K.C., Lenney, M.P., Macomber, S.A., 2001. Classification and change detection using Landsat TM data: when and how to correct atmospheric effects? *Remote Sens. Environ.* 75, 230–244.
- Soudzilovskaia, N.A., Bodegom, P.M., Cornelissen, J.H., 2013. Dominant bryophyte control over high-latitude soil temperature fluctuations predicted by heat transfer traits, field moisture regime and laws of thermal insulation. *Funct. Ecol.* 27, 1442–1454.
- Sundh, I., Mikkilä, C., Nilsson, M., Svensson, B.H., 1995. Potential aerobic methane oxidation in a Sphagnum-dominated peatland—controlling factors and relation to methane emission. *Soil Biol. Biochem.* 27, 829–837.
- Tape, K., Sturm, M., Racine, C., 2006. The evidence for shrub expansion in Northern Alaska and the Pan-Arctic. *Glob. Chang. Biol.* 12, 686–702.
- Tei, S., Morozumi, T., Nagai, S., Takano, S., Sugimoto, A., Shingubara, R., Fan, R., Fedorov, A., Gavrilieva, T., Tananaev, N., 2020. An extreme flood caused by a heavy snowfall over the Indigirka River basin in Northeastern Siberia. *Hydrol. Process.* 34, 522–537.
- Trouet, V., Van Oldenborgh, G.J., 2013. KNMI Climate Explorer: a web-based research tool for high-resolution paleoclimatology. *Tree-ring Res.* 69, 3–14.
- Turetsky, M., Wieder, R., Vitt, D., Evans, R., Scott, K., 2007. The disappearance of relict permafrost in boreal North America: effects on peatland carbon storage and fluxes. *Glob. Chang. Biol.* 13, 1922–1934.
- Turetsky, M.R., Abbott, B.W., Jones, M.C., Anthony, K.W., Olefeldt, D., Schuur, E.A.G., Grosse, G., Kuhry, P., Hugelius, G., Koven, C., Lawrence, D.M., Gibson, C., Sannel, A.B.K., McGuire, A.D., 2020. Carbon release through abrupt permafrost thaw. *Nat. Geosci.* 13, 138–143.
- Updike, T., Comp, C., 2010. Radiometric use of WorldView-2 imagery. Technical Note. DigitalGlobe, pp. 1–17.
- Van Huissteden, J., Maximov, T., Dolman, A., 2005. High methane flux from an arctic flood-plain (Indigirka lowlands, eastern Siberia). *J. Geophys. Res. Biogeosci.* 110.
- Walker, M., Walker, D.A., Everett, K.R., 1989. Wetland Soils and Vegetation, Arctic Foothills, Alaska. US Department of the Interior, Fish and Wildlife Service, Research and....
- Walker, M.D., Walker, D.A., Auerbach, N.A., 1994. Plant communities of a tussock tundra landscape in the Brooks Range Foothills, Alaska. *J. Veg. Sci.* 5, 843–866.
- Wang, J., Zhao, Y., Li, C., Yu, L., Liu, D., Gong, P., 2015. Mapping global land cover in 2001 and 2010 with spatial-temporal consistency at 250 m resolution. *ISPRS J. Photogramm. Remote Sens.* 103, 38–47.
- Wang, P., Mommer, L., van Ruijven, J., Berendse, F., Maximov, T.C., Heijmans, M.M., 2016. Seasonal changes and vertical distribution of root standing biomass of graminoids and shrubs at a Siberian tundra site. *Plant Soil* 407, 55–65.
- Wang, P., Limpens, J., Nauta, A., van Huissteden, C., Quirina van Rijssel, S., Mommer, L., de Kroon, H., Maximov, T.C., Heijmans, M.M., 2018. Depth-based differentiation in nitrogen uptake between graminoids and shrubs in an Arctic tundra plant community. *J. Veg. Sci.* 29, 34–41.
- Wang, P., de Jager, J., Nauta, A., van Huissteden, J., Trofim, M.C., Limpens, J., 2019. Exploring near-surface ground ice distribution in patterned-ground tundra: correlations with topography, soil and vegetation. *Plant Soil* 444, 251–265.
- Wehmann, A., Liu, D., 2015. A spatial-temporal contextual Markovian kernel method for multi-temporal land cover mapping. *ISPRS J. Photogramm. Remote Sens.* 107, 77–89.
- Wein, R.W., 1973. *Eriophorum vaginatum* L. *J. Ecol.* 61, 601–615.
- Westergaard-Nielsen, A., Lund, M., Hansen, B.U., Tamstorf, M.P., 2013. Camera derived vegetation greenness index as proxy for gross primary production in a low Arctic wetland area. *ISPRS J. Photogramm. Remote Sens.* 86, 89–99.
- Zona, D., Oechel, W., Peterson, K., Clements, R., PAW U, K., Ustin, S., 2010. Characterization of the carbon fluxes of a vegetated drained lake basin chronosequence on the Alaskan Arctic Coastal Plain. *Glob. Chang. Biol.* 16, 1870–1882.